THE EFFECT OF FLARE GEOMETRY ON THE FLOW FIELD GENERATED BY RADIAL-RADIAL SWIRLERS

A THESIS SUBMITTED TO
THE GRADUATE SCHOOL OF NATURAL AND APPLIED SCIENCES
OF
MIDDLE EAST TECHNICAL UNIVERSITY

BY

AYŞE BAY

IN PARTIAL FULFILLMENT OF THE REQUIREMENTS
FOR
THE DEGREE OF MASTER OF SCIENCE
IN
AEROSPACE ENGINEERING

JANUARY 2023

Approval of the thesis:

THE EFFECT OF FLARE GEOMETRY ON THE FLOW FIELD GENERATED BY RADIAL-RADIAL SWIRLERS

submitted by **AYŞE BAY** in partial fulfillment of the requirements for the degree of **Master of Science in Aerospace Engineering Department, Middle East Technical University** by,

Prof. Dr. Halil Kalıpçılar
Dean, Graduate School of **Natural and Applied Sciences** _____

Prof. Dr. Serkan Özgen
Head of Department, **Aerospace Engineering** _____

Assist. Prof. Dr. Mustafa Perçin
Supervisor, **Aerospace Engineering, METU** _____

Examining Committee Members:

Prof. Dr. Serkan Özgen
Aerospace Engineering, METU _____

Assist. Prof. Dr. Mustafa Perçin
Aerospace Engineering, METU _____

Prof. Dr. Sinan Eyi
Aerospace Engineering, METU _____

Assist. Prof. Dr. Human Amiri
Aeronautical Engineering, Sivas Sci. & Tech. University _____

Assist. Prof. Dr. Onur Baş
Mechanical Engineering, TED University _____

Date:27.01.2023

I hereby declare that all information in this document has been obtained and presented in accordance with academic rules and ethical conduct. I also declare that, as required by these rules and conduct, I have fully cited and referenced all material and results that are not original to this work.

Name, Surname: Ayşe Bay

Signature :

ABSTRACT

THE EFFECT OF FLARE GEOMETRY ON THE FLOW FIELD GENERATED BY RADIAL-RADIAL SWIRLERS

Bay, Ayşe
M.S., Department of Aerospace Engineering
Supervisor: Assist. Prof. Dr. Mustafa Perçin

January 2023, 53 pages

An experimental investigation is conducted to assess the impact of the flare geometry on the mean flow field generated by radial-radial swirlers. Two-dimensional two-component PIV measurements are performed on the mid-plane of a non-reacting planar combustor test section. A baseline geometry without a flare is compared to four swirlers with three different flare geometries. Analysis of the time-averaged flow fields reveals that there is an increase in radial velocity values and a decrease in axial velocity values as a result of the introduction of the flare geometry, which results in a sudden expansion of the swirling jet. When different flare geometries are compared, almost identical flow fields are observed and the formation of a CRZ is not observed for any configuration that employs a flare geometry. Although the maximum negative axial velocity values decrease for geometries with flare, due to the increase of the recirculation radius, the recirculating mass flow rate is higher than the baseline swirler. On the other hand, the recirculating mass flow rate is higher in the co-rotating swirler configuration due to a stronger adverse pressure gradient along the central axis of the jet when compared to the counter-rotating configuration. High TKE regions are observed at shear layers between the swirling jet and the CTRZ as

well as the swirling jet-CRZ for the Baseline-CR. Regions of high TKE generate intense mixing regions. Coherent flow structures are identified by using the snapshot POD method and different mode shapes obtained for swirlers with and without flare geometry are reported. It is shown that the change in the sense of rotation and flare geometry does not bring about any differences in the POD modes and their energy contents for the given swirl number and confinement conditions.

Keywords: Swirling flow, PIV, flare angle, channel orientation

ÖZ

YÖNLENDİRİCİ GEOMETRİSİNİN RADYAL-RADYAL DÖNDÜRÜCÜ AKIŞ ALANINA ETKİSİ

Bay, Ayşe
Yüksek Lisans, Havacılık ve Uzay Mühendisliği Bölümü
Tez Yöneticisi: Dr. Öğr. Üyesi. Mustafa Perçin

Ocak 2023 , 53 sayfa

Yönlendirici geometrisinin radyal-radyal döndürücüler tarafından oluşturulan ortalama akış alanına etkisini incelemek üzere deneysel bir çalışma yürütülmüştür. 2 boyutlu 2 bileşenli parçacık görüntülemeli hız ölçüm tekniği kullanılmıştır. İzotermal yanma odası test riginde gerçekleştirilen bu testlerde döndürücü çıkışı orta düzleminde ölçüm alınmıştır. Yönlendirici geometrisine sahip olmayan referans döndürücü ile üç farklı yönlendirici geometrisine sahip dört farklı döndürücü birbirleri ile karşılaştırılmıştır. Zaman ortalamalı akış alanları incelendiğinde yönlendirici geometrisinin eklenmesi sonucunda radyal hız bileşeninde artış, eksenel hız bileşeninde azalış gözlemlenmiştir. Bu durum sonucunda döndürücü jetinin ani bir radyal açılım ile duvara yapıştığı gözlemlenmiştir. Birbirinden farklı yönlendirici geometrileri karşılaştırıldığında akış alanında belirgin bir farklılık gözlemlenmemiş, yönlendirici geometrisine sahip hiçbir konfigürasyonda köşe resirkülasyon bölgeleri oluşmamıştır. Yönlendirici geometrisine sahip döndürücülerin yarattığı merkez resirkülasyon bölgelerindeki eksenel hız değerlerinin referansa göre düşük olmasına rağmen daha yüksek resirkülasyon debileri olduğu hesaplanmıştır. Eş-dönüşlü döndürücü tarafın-

dan karşıt yönde güçlü basınç gradyanları yaratılması sebebi ile resirkülasyon debi miktarı ters-dönüşlü konfigürasyona göre daha yüksektir. Yüksek türbülans kinetik enerjisine sahip bölgeler referans döndürücü geometrisi için döndürücü jeti ile merkez resirkülasyon bölgesi ve döndürücü jeti ile köşe resirkülasyon bölgesi arasında kalan katmanlarda gözlemlenmiştir. Yüksek türbülans kinetik enerjisi görülen yerler yanmış ve yanmamış gazların karışımı için karışım yoğunluğu yüksek bölgeler oluşturmaktadır. Koherent akış yapıları enstantane POD metodu ile tanımlanmış ve mod şekilleri referans ile yuvarlatılmış yönlendirici geometrisine sahip döndürücüler için belirlenmiştir. Çalışmaların gerçekleştirildiği hapsetme oranı ve dönüş sayısı koşullarında dönüş yönünün POD modları ve bu modların enerji seviyeleri üzerine bir etkisi olmadığı gözlemlenmiştir.

Anahtar Kelimeler: Döndürücü etkisindeki akış, Parçacık görüntülemeli hız ölçümü, yönlendirici açısı, dönüş yönü

To my parents

ACKNOWLEDGMENTS

I would like to express my gratitude towards my advisor Asst. Prof. Dr. Mustafa Perçin. I have learned so much throughout this process. His guidance was not only limited to his academic knowledge but also thought me so much about being a better person. His dedication, discipline, and honesty will always be qualities that I look up to.

Next, I would like to thank my mentor Fırat Kıyıcı. The support he gave me throughout this study is beyond perception. Whenever I needed help, regardless of the problem, he gave me guidance and the greatest advice, told me the best anecdotes & sent me the funniest videos for a late-night giggle. I owe you big time.

The help of my dear friend Ahmet Kaan Zayim on the flawless mechanical design and thorough post-production inspection of the test specimen is much appreciated. Special thanks to Battal Gencer for being there during my first experiments, showing me around, and introducing me to the test article. I would also like to thank TUSAS Engine Industries Inc. for their financial support & the RUZGEM personnel for their technical assistance.

Last but not least, I would like to thank my family for their unconditional support. The motivation they constantly provided me with, kept my spirits high and helped me complete what I have started. Thank you for being there for me through the good times and the bad.

TABLE OF CONTENTS

ABSTRACT v

ÖZ vii

ACKNOWLEDGMENTS x

TABLE OF CONTENTS xi

LIST OF TABLES xiii

LIST OF FIGURES xiv

LIST OF ABBREVIATIONS xvii

CHAPTERS

1 INTRODUCTION 1

1.1 The impact of the flare geometry 6

1.2 Turbulence, coherent structures and mode identification 8

1.3 Motivation and problem definition 16

1.4 The outline of the thesis 17

2 METHODOLOGY 19

2.1 Experimental method 19

2.2 Swirler geometries 20

2.3 Experimental facility 22

2.4 Particle image velocimetry test setup 23

2.5 Uncertainty analysis 26
2.6 Proper orthogonal decomposition 27
3 RESULTS 29
3.1 Effect of flare expansion 31
3.2 Effect of flare geometry 38
3.3 Effect of channel orientation 41
3.4 POD results 42
4 CONCLUSIONS 47
REFERENCES 49

LIST OF TABLES

TABLES

Table 2.1 Swirler geometrical properties 22

Table 2.2 Test section entrance properties [1] 24

Table 2.3 Vector spacing of PIV images 26

Table 2.4 Statistical uncertainties in first- and second-order components for 95% confidence interval 27

Table 3.1 Normalized recirculating mass flow rate and CTRZ width values of various swirler geometries 40

LIST OF FIGURES

FIGURES

Figure 1.1 The thermodynamic Brayton Cycle [2] 1

Figure 1.2 Schematic of a combustor's parts and the flow inside of it [3] . . 2

Figure 1.3 Simple sketch of flow field generated by dual-flow swirlers inside a combustor [4] 3

Figure 1.4 Axial and radial swirlers [5] 4

Figure 1.5 A dual-flow radial-radial swirler with flare expansion [6] 7

Figure 1.6 The flare expansion angle 7

Figure 1.7 Time averaging parameters [7] 9

Figure 1.8 Kolomogorov energy spectrum of turbulent flows[8] 11

Figure 1.9 Modal decomposition of 2D incompressible flow over a flat plate [9] 12

Figure 1.10 Representation of PVC [10] 14

Figure 1.11 Anti-symmetric flow structure represented in terms of radial velocity component [11] 14

Figure 1.12 Average flow field and POD modes of different operating conditions of the same burner geometry [12] 16

Figure 2.1 Schematic of a PIV setup in a wind tunnel [13] 20

Figure 2.2 2D and 3D drawings of the swirler with flare geometry 21

Figure 2.3 Swirler geometries 23

Figure 2.4 Experimental facility 24

Figure 2.5 Thin and aligned laser sheet at mid-plane of the swirler exit . . . 25

Figure 2.6 Swirler placements inside the test section and measurement plane 26

Figure 2.7 Axial velocity profiles of the Rad-CR swirler at $y/D_h = 1$ for 10, 100, 1000 and 2000 image pairs 27

Figure 2.8 PIV Test Setup 28

Figure 3.1 Direct comparison of experimental and numerical study data of the time-averaged flow field generated by the Rad-CR swirler 30

Figure 3.2 Comparison of axial velocity profiles obtained for the Rad-CR swirler at $y/D_h = 1$ via CFD and experiments 31

Figure 3.3 Time-averaged velocity fields in y-direction for Baseline-CR (left) and Rad-CR (right) swirlers 32

Figure 3.4 Normalized TKE ratio contour of Baseline-CR (left) and Rad-CR (right) swirlers 33

Figure 3.5 Time-averaged axial and radial velocity components at $y/D_h = 0.5, 1\&2$ of the Baseline-CR and Rad-CR swirlers 35

Figure 3.6 Comparison of axial velocity profiles obtained for the Rad-CR swirler via CFD and experiments at various streamwise locations 36

Figure 3.7 Numerical results of axial pressure gradients at the symmetry axis of the Baseline-CR and Rad-CR swirlers 37

Figure 3.8 Numerical results of velocity components at flare exit of the Rad-CR swirler 38

Figure 3.9 Time-averaged velocity fields in y-direction for 27.5CH-CR, 45CH-CR, and Rad-CR swirlers 39

Figure 3.10 Time-averaged axial and radial velocity components at $y/D_h = 0.5, 1\&2$ of the 27.5CH-CR, 45CH-CR, and Rad-CR swirlers 40

Figure 3.11 Time-averaged velocity fields in y-direction for Rad-CR (left), Rad-CO (right) swirlers 41

Figure 3.12 Normalized TKE ratio contour of Rad-CR (left), Rad-CO (right) swirlers 42

Figure 3.13 Time-averaged axial velocity components at $y/D_h = 0.5, 1\&2$ of the Rad-CR and Rad-CO swirlers 43

Figure 3.14 Energy modes for different flare geometries 44

Figure 3.15 Representation of the first five POD modes in descending order by means of contours of the velocity component in the y-direction for the Baseline-CR (left), Rad-CR (middle), and Rad-CO (right) swirlers . 45

LIST OF ABBREVIATIONS

2D2C	2 Dimensional 2 Component
2D	2 Dimensional
3D	3 Dimensional
CTRZ	Central Toroidal Recirculation Zone
CRZ	Corner Recirculation Zone
PIV	Particle Image Velocimetry
PVC	Precessing Vortex Core
POD	Proper Orthogonal Decomposition
R_{po}	Primary Channel Outer Radius
R_{so}	Secondary Channel Outer Radius
R_{si}	Secondary Channel Inner Radius

CHAPTER 1

INTRODUCTION

Gas turbines are frequently used in engineering for power and thrust generation. Applications can vary from industrial to aviation purposes. The thermodynamic principle behind the gas turbine is known as the Brayton Cycle. The simple Brayton Cycle comprises air pressurization, heat addition to the pressurized air, and work extraction from the heated air as depicted in Fig. 1.1. The remaining energy after this process can be used for thrust generation via propelling nozzles or power generation with the help of a power absorber. The amount of energy remaining strictly depends on the heat added to the system. Therefore, the design of the combustor is an important part of any gas turbine project, and it is desired to obtain the most efficient combustion with the least amount of loss in pressure.

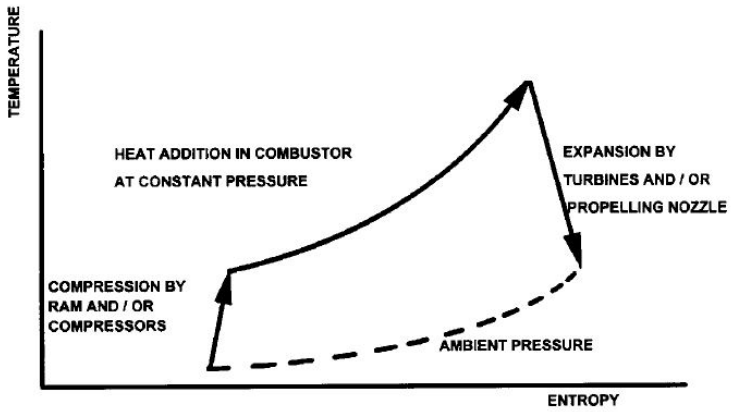


Figure 1.1: The thermodynamic Brayton Cycle [2]

Modern combustors consist of several parts which serve different aspects of achieving the most efficient temperature rise. Generally, an air casing, a diffuser, a liner,

and fuel injectors exist in all combustor chamber designs. The diffuser slows down the air coming from the compression process which serves as an initial preparation for it to be combusted. If a diffuser was not incorporated and the combustion was to be made inside a straight pipe, there would be an unacceptable amount of pressure loss. Another necessity of the combustor is to fix the flame position by generating a region of recirculation. This low-speed region prevents the flame from elongating and leaving the combustor together with the air moving out of it. The liner is employed to assure only a portion of the air within the flammability limits of the used fuel enters the combustion process whereas the rest enters the chamber at more downstream locations. These are stated as the key elements of a gas turbine combustion chamber [5], but more sophisticated designs are added to this base configuration to achieve the design requirements of the combustor. A schematic of the parts of a combustor and the flow inside of it is given in Fig. 1.2.

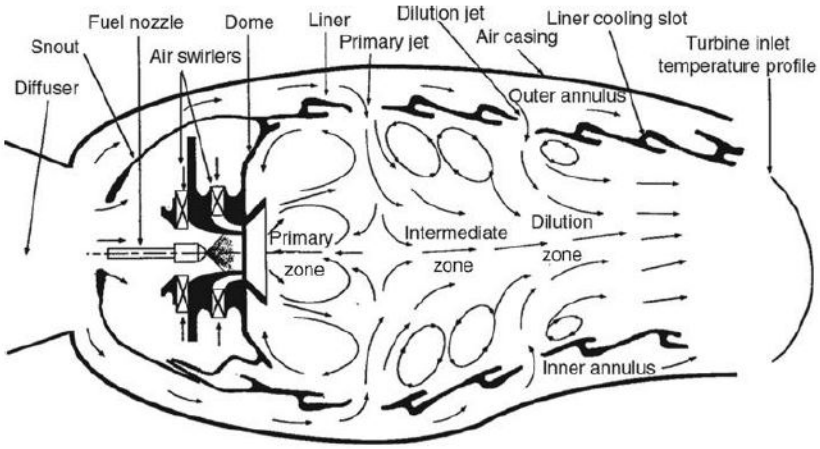


Figure 1.2: Schematic of a combustor's parts and the flow inside of it [3]

The primary zone is usually where the flame is anchored. The flow inside the primary zone must be such that there is sufficient time, mixing, turbulence, and temperature to complete the chemical combustion reaction. Several ways exist to assure flame stabilization which is of critical importance in gas turbine combustors. The common feature of these methods is the generation of the toroidal recirculation zone where hot combustion products are mixed with freshly entrained air and fuel [5]. The flow field generated by a cylindrical bluff body, the integration of the V-gutters, and the initia-

tion of vortex breakdown are common examples of methods in the literature. However, generating recirculation regions by vortex breakdown is advantageous over other methods, due to the strong shear regions produced by swirl components contributing to increased turbulence levels and mixing rates [5]. Swirl-stabilized combustion produces higher rates of entrainment of the surrounding fluid and assures rapid mixing close to the exit nozzle as well as the recirculation zone boundaries helping to reduce the combustion lengths [14].

The vortex breakdown phenomena can be initiated with the help of swirling flows. Introducing a rotating motion to a fluid upstream of an orifice generates a tangential velocity component which makes it different than a normal jet flow. The presence of the tangential velocity component causes pressure gradients in axial and radial directions. With a sufficiently high tangential velocity, a strong adverse axial pressure gradient can be obtained which will cause flow reversal. [15]. A simple sketch of the flow generated by swirlers inside a combustor is shown in Fig. 1.3.

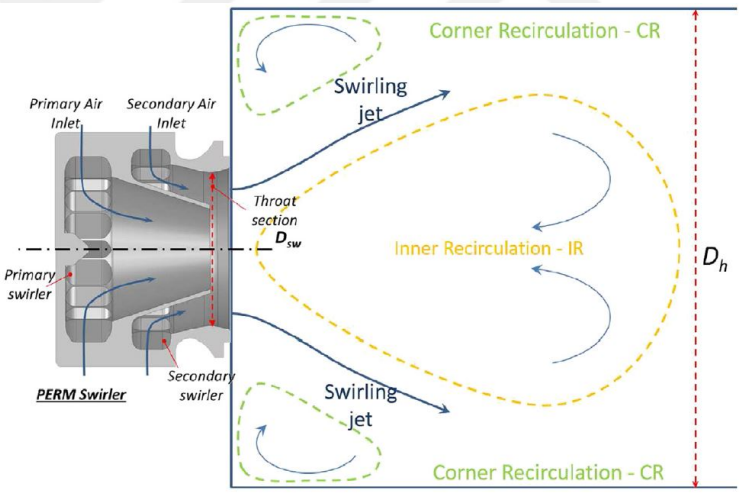


Figure 1.3: Simple sketch of flow field generated by dual-flow swirlers inside a combustor [4]

Swirlers can be designed to direct the airflow to the primary zone either axially or radially. Axial swirler applications are more common in the aero-engine industry. A simple schematic of axial and radial swirlers is given in Fig. 1.4. Moreover, the swirlers can be designed to have single or double passages in which case they generate co- or counter-rotating flows. Axial and radial passages can also be combined in the

case of double-passage (i.e. dual-flow) swirlers.

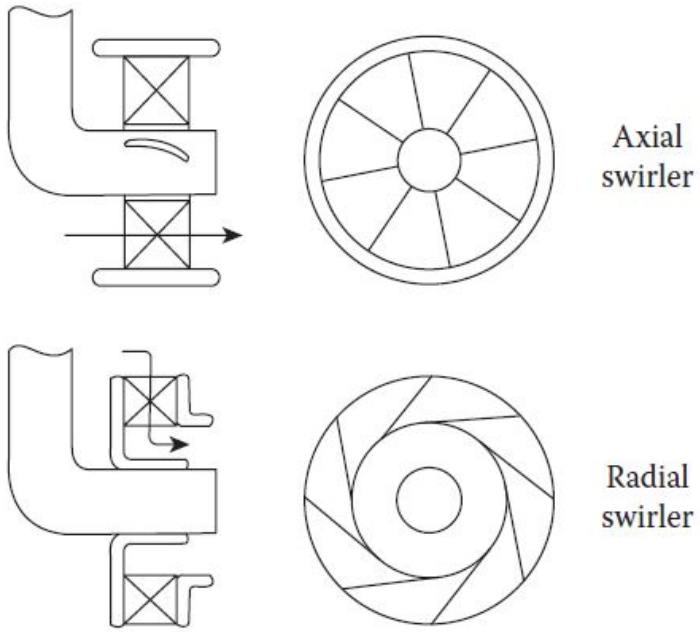


Figure 1.4: Axial and radial swirlers [5]

There are several design parameters influencing the flow field generated by swirlers. Some of these are listed as follows

- Swirl number
- Swirler type (axial or radial)
- Direction of rotation
- Flow split ratio
- Confinement ratio
- Flare angle
- Chamber length
- Dome geometry
- Reynolds number

- Outlet conditions

Extensive experimental and numerical research is carried out on each of these design parameters. The flow field generated by two different double-passage swirlers was investigated by Kao et. al. [16]. A co-axial counter-rotating radial-radial swirler was compared to an axial-radial swirler. The Laser Doppler Velocimetry (LDV) experiments revealed that the radial-radial swirler had an open-shape Central Toroidal Recirculation Zone (CTRZ) due to the highly dispersing characteristic of the flow under unconfined conditions. The flow of the radial-radial swirler was attached to the dome whereas the swirling jet expansion angle was lower for the axial-radial swirler.

The channel orientation was studied by Merkle et. al. [17], Kıyıcı and Perçin [1], Kilik and Finstad [18]. In general, it was observed that for the co-rotating configuration, the axial length of the recirculation zone increases whereas the recirculating mass flow rate decreases. The interaction between the co-rotating channel flows prevents a shear layer from forming between the two flows which lowers the dissipation of the tangential momentum. Larger swirling jet expansion angles are observed for co-rotating configurations. The effect of confinement was studied by Kıyıcı and Perçin [1] for high swirl number applications whereas Fu et. al. [19], [20] investigated low swirl number cases. As the confinement ratio decreases, the expansion of the swirling jet increases. The highest turbulence is observed for the smallest confinements.

Gencer et. al. [21] performed an experimental study to investigate the effect of the channel geometry as well as the number of passages by keeping all other design parameters of the swirler to be the same. The number of passages was not found to have a significant effect on the time-averaged flow field given the conditions and other design parameters of the investigated cases. However, they have shown that the square-shaped vanes have narrower swirling jet expansion angles making the width of the CTRZ smaller.

Other than the geometry of the swirler, the downstream conditions also have an impact on the flow field generated. Kao et. al.[6] studied the effect of the chamber length by conducting 2 component LDV measurements on a non-reacting test rig. As the chamber length decreases, the flow would be accelerated by a favorable pressure gradient along the axis of the swirler. This increased the axial and tangential velocity

magnitudes inside the swirling jet.

Some studies aimed to understand the conditions under reactive conditions. Merkle et. al. [22] focused on the mechanisms which make the counter-rotating (CR) swirler have a larger operating range when compared to the co-rotating (CO) configuration. The additional vortex formed at the nozzle vicinity as well as the dampening effect of the tangential velocity profiles causes the mixing rates to increase. Near-stoichiometric conditions are obtained for larger areas which widen the operational envelope of the CR swirler. Marinov et. al. [23] compared swirl-stabilized flow fields in isothermal and reactive conditions. They observed that the formation of an inner and outer recirculation region is observed in both cases. While the shape of the inner recirculation zone changes (closes in reacting conditions), the general flow structure and the outer recirculation regions do not vary between isothermal and reacting conditions. Cai et. al. [24] used flow imaging techniques to assess the dynamics of the combustion process. Dynamics related to the fuel-lean and fuel-rich regions were studied. Whereas the fuel-rich modes were related to the interaction between the unburnt fuel and the dilution jet, the fuel-lean modes were attributed to the unsteady swirling flow.
It is obvious that different parameters have been the interest of numerous studies. The next section focuses on the studies conducted to understand the impact of the flare expansion geometry which will help to explain the motivation behind the current study.

1.1 The impact of the flare geometry

The flare geometry is an extension to the swirler exit which directs the flow at a certain angle before leaving the swirler. A dual-flow swirler cup with flare expansion is shown in Fig. 1.5. Different flare geometries can exist including filleted and chamfered flare geometries. In the case of chamfered flare geometries, a flare expansion angle can be defined from the vertical axis passing through the center of the swirler as shown in Fig. 1.6. A limited number of studies investigated the effect of the flare expansion angle on the flow field generated by swirlers.

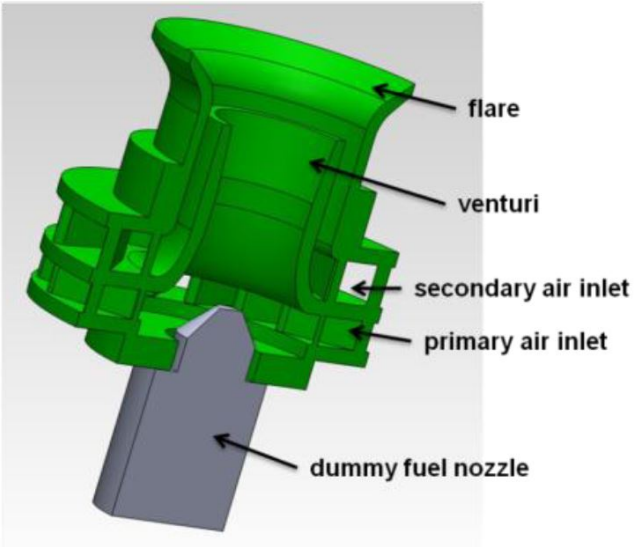


Figure 1.5: A dual-flow radial-radial swirler with flare expansion [6]

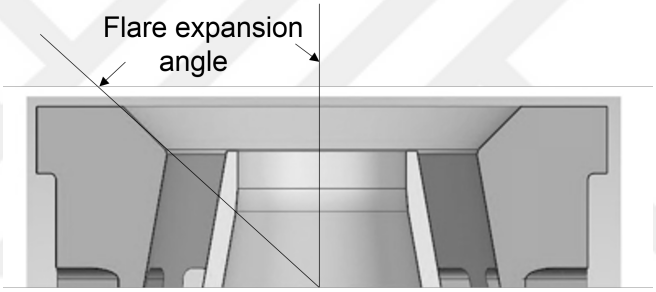


Figure 1.6: The flare expansion angle

Estefanos et. al. [25] conducted 2D high-speed Particle Image Velocimetry (PIV) measurements in a water test rig. Their UCRI 2 swirler had a design (theoretical) swirl number of 0.64 [26], a ratio of confinement area to swirler exit area (i.e. confinement ratio) of 5.1 [26], [27] and was tested in isothermal conditions. Three flare expansion angles of 30.9°, 35.9°, and 40.9°were studied. They have analyzed both mean flow quantities as well as dynamic behavior changes with the help of temporal Fast Fourier Transform (FFT) analysis. In their mean flow field results, they have obtained that the jet expansion angle increases together with increasing flare expansion angle. A larger flare angle increases the radial velocity component magnitude and lowers the axial velocity magnitude at the swirler exit as well as at downstream locations until the swirling jet becomes a wall jet. Moreover, when they compared their results with a previous study of the same swirler without flare [27], they have seen

that the swirling jet expansion is restricted with the addition of the flare geometry. In their dynamic analysis, they found that for the narrowest flare expansion angle, there are two instability regions and four exist for the wider flare angles. They claim that a circumferential mode of instability reveals itself due to a phase difference of 3.14 radians between the high Turbulence Kinetic Energy (TKE) regions.

It is difficult to find other contemporary studies focusing on the effect of the flare geometry. However, Wang et. al. [28] published an experimental study in 1995 comparing the flow field generated by swirlers with two different flare angles. They performed two component Phase Doppler Particle Analyzer (PDPA) measurements on the CFM56 swirl cup for unconfined conditions. Continuous phase velocity results are extracted from statistics obtained for particles with smaller diameters than 4.17 μm. They have observed that the wider flare angle (60°) constructs a wider recirculation zone with lower recirculating speeds when compared to the narrow flare angle (45°). At downstream locations, the wide flare stream sweeps the surrounding air into the recirculation zone causing the recirculating mass flow rate to be larger than the injected mass flow rate. The mean axial, radial, and tangential velocity components of the wide flare are smaller due to dissipation at the swirler exit. The flow attaches to the dome and is not restrained by the shear layer as it was for the narrow flare.

It can be seen that the number of studies interested in flare expansion geometry is rather limited. Unconfined and low confinement cases were investigated with relatively low swirl numbers. Further investigation in this area is needed for a better understanding of the impact of the flare geometry on the flow field generated by radial-radial swirlers.

1.2 Turbulence, coherent structures and mode identification

Swirling flows are highly turbulent by nature. Turbulent flow is a 3D flow that is essentially unsteady. The quantities of the flow are random functions of time and space however, they have statistical averages which are considered to be deterministic. The properties of the turbulent flows are still obtained using the Navier-Stokes equations given in Eq. 1.1 and Eq. 1.2 which are written for incompressible fluid

flow in isothermal conditions with negligible body forces.

$$\frac{\partial \rho}{\partial t} + \frac{\partial \rho U_i}{\partial x_i} = 0 \tag{1.1}$$

$$\frac{\partial (\rho U_i)}{\partial t} + \frac{\partial (\rho U_i U_j)}{\partial x_j} = -\frac{\partial p}{\partial x_i} + \frac{\partial \tau_{ij}}{x_j} \tag{1.2}$$

The turbulent flow quantities can be represented in terms of time-averaged ($\overline{Q_i}$) and fluctuating (q_i) components as was done by Reynolds. This procedure is called Reynolds averaging formulated as in Eq. 1.3 with Q_i being any quantity of the flow.

$$Q_i = \overline{Q_i} + q_i \tag{1.3}$$

The time-averaged quantity $\overline{Q_i}$ is defined as given in Eq. 1.4 by using the averaging parameters depicted in Fig. 1.7. Here, the time T is the period over which the time average of all the fluctuating components is zero.

$$\overline{Q_i} = \frac{1}{T} \int_t^{t+T} Q_i(\tau) d\tau \tag{1.4}$$

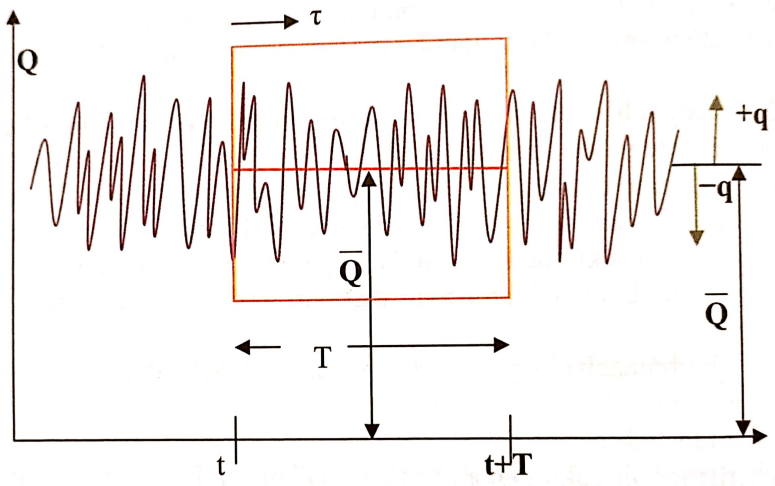


Figure 1.7: Time averaging parameters [7]

Applying the Reynolds decomposition to the equations given in 1.1 and 1.2, one can obtain the Reynolds Averaged Navier Stokes Equations (RANS) as in Eq. 1.5 and 1.6, which converts a problem with 4 equations (1 continuity and 3 momentum conservation equations) and 4 unknowns (velocity components & pressure), to a problem of 4 equations and 13 unknowns where 9 of these unknowns are components of the Reynolds stress tensor.

$$\frac{\partial \rho}{\partial t} + \frac{\partial \rho U_i}{\partial x_i} = 0 \tag{1.5}$$

$$\frac{\partial (\rho U_i)}{\partial t} + \frac{\partial (\rho U_i U_j)}{\partial x_j} = -\frac{\partial p}{\partial x_i} + \frac{\partial (\tau_{ij} - \rho \overline{u_i u_j})}{x_j} \tag{1.6}$$

The additional terms $\rho\overline{u_i u_j}$ is the 3×3 Reynolds stress tensor. Methods based on the solution of the Reynolds stresses in numerical analysis are various turbulence modeling techniques used in conjunction with RANS equations. Similarly, this averaging can be done in the spatial domain which is the basis of LES numerical modeling. It can be concluded that turbulent flows are difficult to deal with and thus a source of interest to many researchers who conduct experimental and numerical studies to be able to understand the flow quantities and dynamics.
The turbulent flow consists of many eddies. Eddies can be defined as a grouping of specific molecules which choose to stay together for a limited time. They form or keep the identity (i.e. the kinetic energy and momentum) of the group, before transmitting their energy and forming other structures. The size and energy content of the eddies can be graphed as in Fig. 1.8.

The scale with the most energy-containing structures is called the integral scale. Eddies in the integral scale, disperse and construct smaller eddies which also exist for a certain time and disperse. This process continues and the smallest eddies formed during this dispersion are affected by the viscosity which causes them to dissipate into heat. The dissipation due to viscosity takes place in the Kolmogorov scale. However, the amount of energy that is dissipated is not in direct relation to the viscosity. Viscosity only determines the scale at which dissipation occurs. The amount of energy that dissipates is determined by the larger energy-containing structures which gained

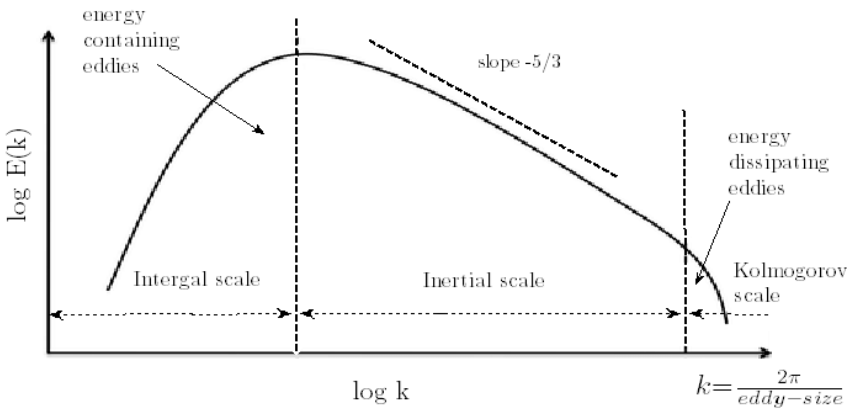


Figure 1.8: Kolomogorov energy spectrum of turbulent flows[8]

their energy from the mean flow. In other words, the rate at which energy is transmitted from the mean flow to the turbulence, and at which it leaves from larger eddies forming smaller ones in the flow is determined by large-scale dynamics. When the energy reaches the smallest scales, the rate of dissipation can no longer be affected. Understanding the large-scale dynamics of the flow is therefore of great importance. The most evident structures are exhibited in these energy-containing large scales and are called coherent structures [29].

Coherent structures are energetically dominant structures that repeat their presence in flow periodically. They are usually formed as a result of local flow instabilities [30]. Different from eddies, coherent structures can not be superimposed or do not transmit their energy to smaller eddies. Their interaction forms other structures of various scales. In order to fully and realistically encompass the motions of different sizes inside of a turbulent flow, the flow field needs to be decomposed into mean and a hierarchy of both coherent and incoherent motions of various scales [30].

In order to identify coherent structures, it is common practice to deploy modal analysis. With modal analysis, dominant features of a fluid flow in terms of energy level can be extracted. The flow features are represented by a set of spatial modes and energy content levels (or growth rates and frequencies) associated with those spatial modes. In Fig. 1.9 results of a POD analysis are given on a laminar separated 2D flow over a flat plate [9]. By investigating the instantaneous flow field, the formation of the Karman-vortex street can be observed. This can be mathematically expressed by the

time-averaged flow field combined with two of the most energetic modes found when the modal analysis is applied. As it can be seen from the reconstructed flow in Fig. 1.9, for the given case the instantaneous flow field can be realistically anticipated by only two of the oscillatory modes.

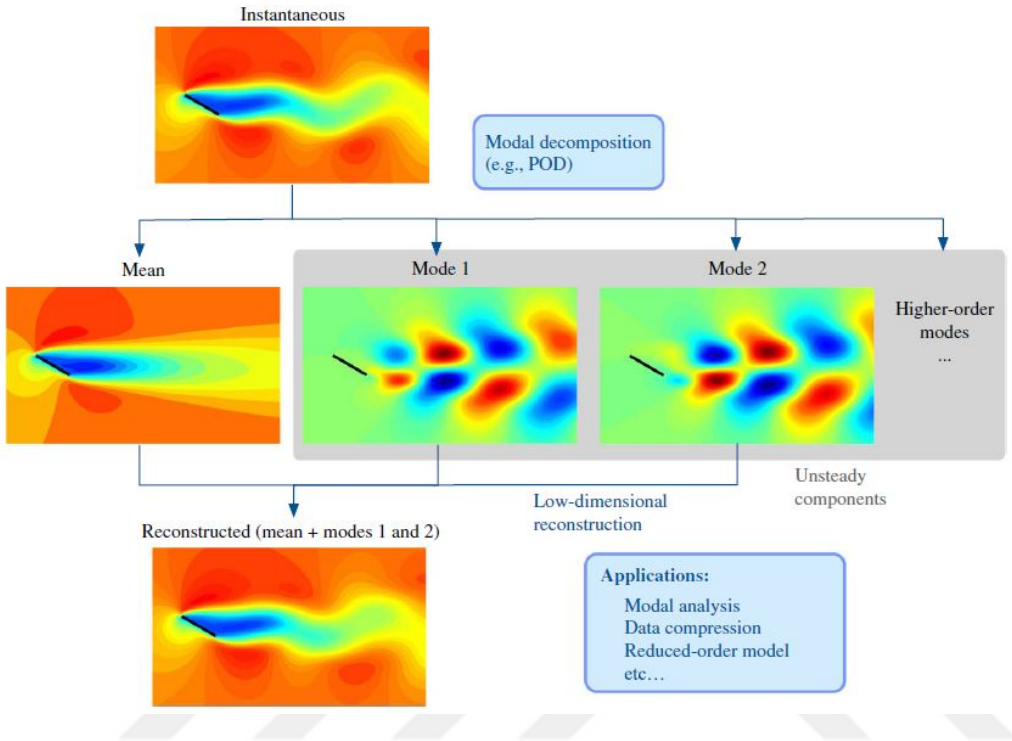


Figure 1.9: Modal decomposition of 2D incompressible flow over a flat plate [9]

Modal decomposition techniques are based on the eigenvalue decomposition of matrices. The eigenvalues and eigenvectors of a matrix capture the directions in which vectors can grow or shrink [9]. The vector v and the scalar λ of an $n \times n$ square matrix A are said to be its eigenvector and eigenvalue if the relation in Eq. 1.7 holds. This expression means that if an operator A is applied to its own eigenvector, this operation can be defined by simply multiplying the eigenvector v with a scalar λ associated with that eigenvector.

$$Av = \lambda v \tag{1.7}$$

Supposing that A has n linearly independent eigenvectors ($V = [v_1, v_2, ...v_n]$) and eigenvalues ($\Lambda = diag(\lambda_1, \lambda_2, ..., \lambda_n)$) associated with the eigenvectors, then Eq. 1.7

can be extended into Eq. 1.8

$$AV = V\Lambda \tag{1.8}$$

The eigenvalue problem is solved by post-multiplying each side of Eq. 1.8 by the inverse of the eigenvector matrix as shown in Eq. 1.9. This procedure is called eigenvalue decomposition.

$$A = V\Lambda V^{-1} \tag{1.9}$$

Proper orthogonal decomposition (POD) method and its derivatives, dynamic mode decomposition (DMD), global linear stability analysis, etc. are modal analysis methods based on the solution of the above-mentioned eigenvalue problem. The most frequently used method in fluid flow is the POD analysis. The POD technique aims to decompose a given set of data into a minimum number of modes (or basis functions) so that the limited number of modes captures as much energy as possible. Once the eigenvalue problem is solved, the eigenvalues are arranged from largest to smallest ordering the modes in terms of the kinetic energy level of the flow field. The snapshot POD method is a derivative of the classical POD method suggested by Sirovich [31]. Instead of solving the eigenvalue problem in the entire spatial domain of $n \times n$, the snapshot POD method uses m number of snapshots capturing the important fluctuations in the flow field and solves the $m \times m$ eigenvalue problem. Another variation of the classical POD analysis is the spectral POD proposed by Lumley [32]. The spectral POD provides a set of modes with discrete frequencies rather than mixed frequencies. This is achieved by applying temporal Fourier Transform on the flow field data before extracting the spectral POD modes.

Extracting the coherent structures of swirl-flow-generated vortex breakdown is of great importance. In literature swirl induced vortex breakdown is said to be followed by a global flow instability called the Precessing Vortex Core (PVC) [33]. The PVC is a helical flow structure wrapping itself around the reverse flow boundary [10]. The center of the vortex is different from the center of the swirler. A representation of the PVC can be seen in Fig. 1.10.

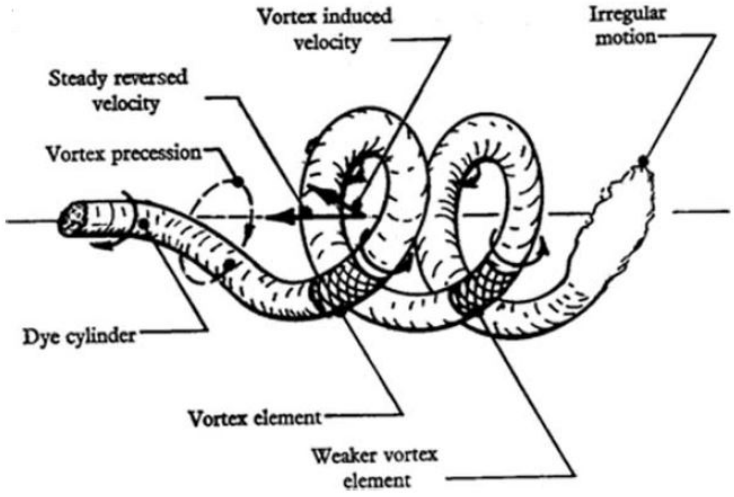


Figure 1.10: Representation of PVC [10]

Many researchers focus on the identification of the PVC mode in swirl-stabilized combustors. Sieber et. al. [11] developed an improved POD analysis that they have called Spectral POD analysis (S-POD, different from the previously explained spectral POD) in order to extract the dominant modes of swirling flow inside a combustor. When represented in terms of the radial velocity component, the PVC has an anti-symmetric structure as shown in Fig. 1.11.

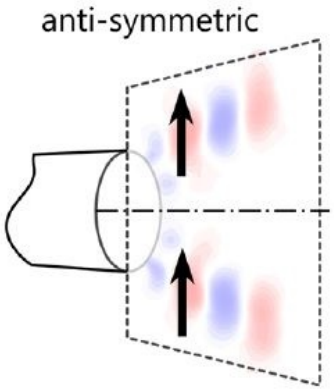


Figure 1.11: Anti-symmetric flow structure represented in terms of radial velocity component [11]

Sieber et. al.[11] conducted SPOD on the PIV measurements and compared the per-

formance of POD and SPOD. They have captured modes that resemble the PVC I mode. However, with the SPOD method, the PVC I mode had a better-defined peak in the frequency spectrum. They have concluded that the SPOD method generates results for which it is easier to relate the modes with their physical interpretations.

Terhaar et. al. [33] conducted an experimental and numerical study to investigate the influence of the vortex breakdown type on the global modes in swirling flow. The POD results on the experimentally obtained isothermal & reacting cases reveal that similar vortex patterns along the inner shear layers are observed in both cases. As they injected air axially, they observed that the dominant mode shifted from PVC type I to PVC type II. Moreover, comparing the reacting and isothermal results, they found that the frequency of the self-excited oscillation is not influenced by combustion.

Oberleithner et. al. [12] conducted an experimental study on the effect of the presence and shape of the flame on the suppression of the PVC in a swirl combustor. Applying POD analysis to the obtained results they have seen that in all isothermal conditions, the presence of the PVC is manifested over a range of modes. However, when the reacting conditions were investigated, the formation of the PVC was not always observed in the most energetic 3 modes as shown in Fig. 1.12. The presence of the PVC was linked to the flame shape (i.e. the operating condition of the burner). In case of the isothermal and M-shaped flame conditions (A and C respectively), the first two modes represent the coherent helical PVC located at the inner shear layer. For the V-shaped flame (denoted as Case B) however, the energy content of the most energetic modes is significantly lower, and there are no vortex patterns observable in the inner shear layers.

To conclude, it is important to understand the dynamic changes in the flow initiated by varying the swirler design parameters. A POD study is conducted in this thesis to identify mode structures with the addition and variation of the flare expansion geometry.

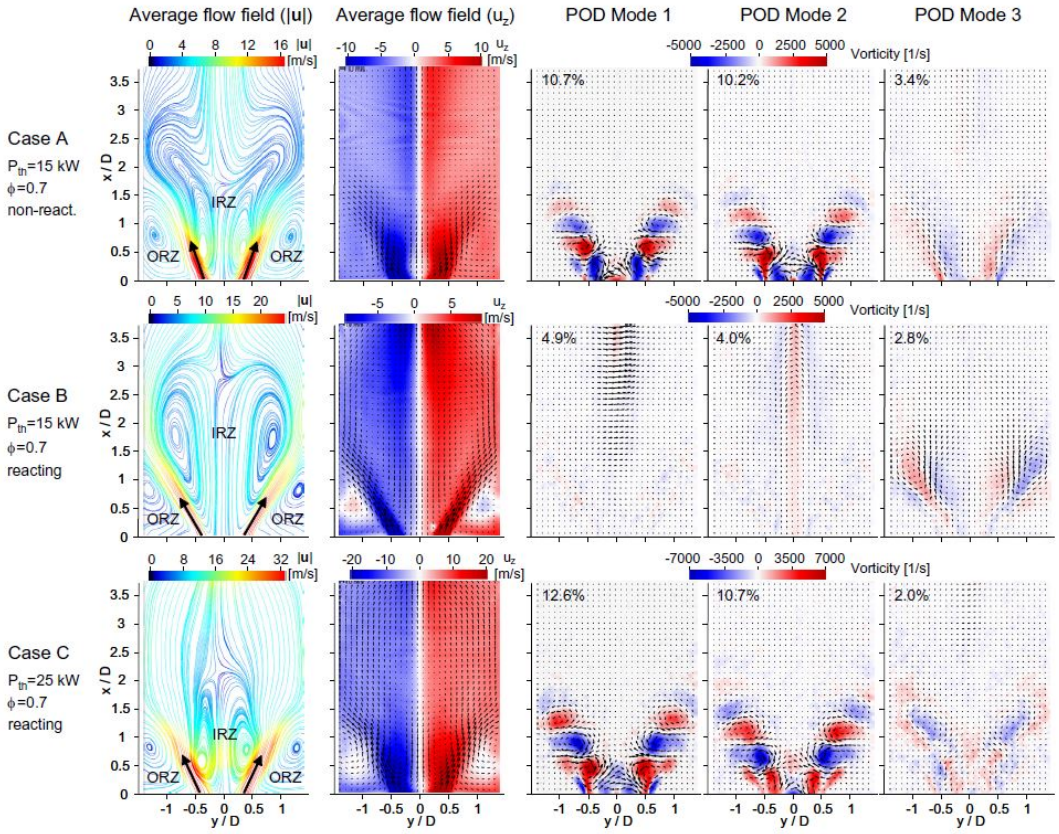


Figure 1.12: Average flow field and POD modes of different operating conditions of the same burner geometry [12]

1.3 Motivation and problem definition

There is extensive knowledge in literature focusing on the effect of changing design parameters of swirlers on the flow fields generated by them. Researchers focused heavily on parameters such as the confinement ratio, the channel orientation, the swirl number, etc. However, there is a limited number of studies focusing on the impact of the addition and variation of the flare geometry on the flow field generated by radial-radial swirlers. Moreover, the existing studies restrict their investigations to low swirl numbers, low confinement, or unconfined cases. The identification of mode shapes of the swirling flow generated by swirlers employing a flare geometry is not studied extensively in the field. The current study aims to contribute to these aspects by presenting two-dimensional two-component Particle Image Velocimetry (2D2C PIV) results conducted on the flow field generated by co- and counter-rotating radial-radial

swirlers in isothermal conditions where swirl number & confinement ratio are fixed.

1.4 The outline of the thesis

This thesis presents the results of an experimental investigation conducted to understand the impact of the flare geometry on the flow field generated by radial-radial swirlers. It is constructed of four chapters. In the first one, some introductory knowledge is shared regarding gas turbine applications, combustors and their working principles, flow structures generated by swirlers, etc. Studies found in literature focusing on the effect of flare geometry are mentioned before concluding with the motivation behind the current study and the thesis outline. The second part elaborates on the experimental methodology applied. Some theoretical information regarding the concept of Particle Image Velocimetry (PIV) is given. The swirler geometries under investigation are depicted and their design parameters are provided. Moreover, the experimental facility and setup are introduced giving insight into all the necessary equipment. The methodology behind the uncertainty and POD analyses applied to the test data obtained in this study is explained. The next section presents all the experimental results that are obtained. The addition of the flare geometry, the variation of flare geometry, and the channel orientation effects are studied explicitly. Results of the POD analysis are shared and identification of the mode shapes is conducted at the end of this section. Finally, in the last part, the findings of the study are summarized, and the most important outcomes of the study are stated.

CHAPTER 2

METHODOLOGY

In this section, the details related to the experimental setup are presented. First, the experimental method is introduced. Next, details about the swirler geometries under investigation are given. A thorough introduction to the test chamber as well as the PIV setup is provided. The uncertainty of the experimental results is shown to support the reliability of the obtained data. Finally, the methodology of the proper orthogonal decomposition is explained.

2.1 Experimental method

Particle Image Velocimetry (PIV) is a quantitative, non-intrusive measurement technique used in experimental fluid mechanics. Sufficiently small tracer particles are introduced to the flow in order to move along with it. A source of light illuminates these particles and causes them to scatter light. A visual recording device, such as a high-speed camera, captures the light scattered by the particles at least twice with a short time period between them. A comparison of two consecutive captures reveals the motion of the flow of interest.

Whereas most of the experimental techniques allow velocity measurement of a single point in the flow, the images captured during PIV have a large spatial resolution. In planar PIV, a 2-dimensional laser sheet is generated within the flow, and the illuminated sheet is recorded. To analyze the motion, these images are divided into smaller interrogation windows. Each interrogation window includes a number of particles that are assumed to move homogeneously. Local velocity vectors of all particles are calculated and a single velocity vector describing the motion of the flow inside that

interrogation window is generated with the use of statistical methods such as cross-correlation.

The components of a PIV measurement system inside a wind tunnel are given in Fig. 2.1 [13]. Laser sheet optics are used to generate a thin layer of light and reflect on the flow area of interest with the help of mirrors. Imaging optics (lenses) focus on the particles to obtain high-quality images which are easier to analyze with statistical methods when compared to blur images. Usually, a synchronizing device is used to arrange the times of laser pulses, image capturing, and data transmission to the computers. Instantaneous images of the flow phenomenon under investigation are taken at times t and t' which can then be analyzed with several different methods, without the need of repeating the experiments.

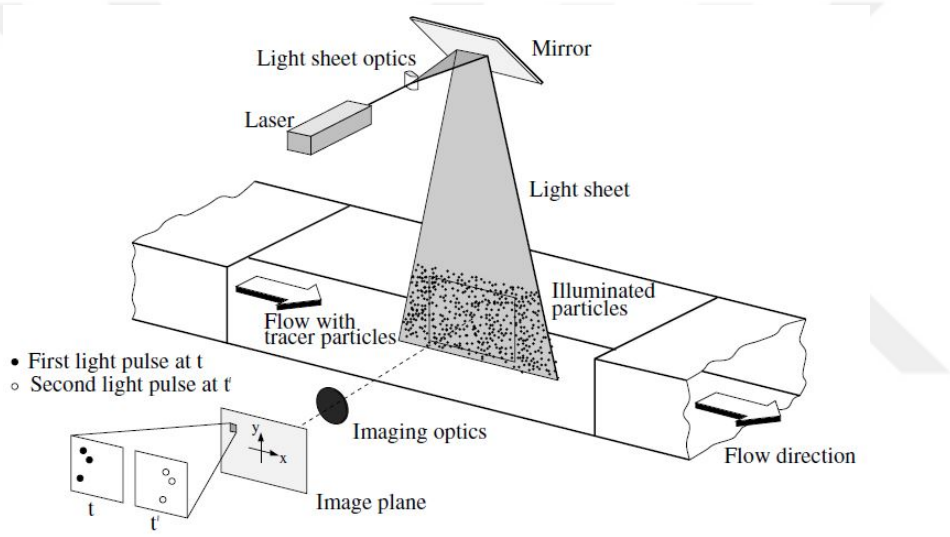


Figure 2.1: Schematic of a PIV setup in a wind tunnel [13]

2.2 Swirler geometries

In this study, the flow fields of five different swirler geometries are investigated experimentally. In order to study the effect of the flare expansion geometry on the flow field generated by radial-radial swirlers, all other design parameters were set to be identical except for the flare expansion geometry. Each of the swirlers has 8 primary and 12 secondary channels. Whereas 28% of the flow passes through the primary vanes, the remaining 72% flows through the secondary vanes. The schematic of the

swirlers is given in Fig. 2.2.

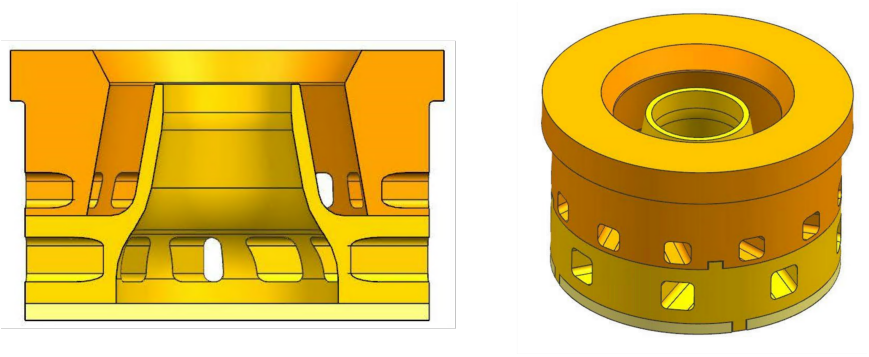


Figure 2.2: 2D and 3D drawings of the swirler with flare geometry

The design of the swirlers is such that they yield identical swirl numbers of value 1.2. The swirl number of the primary and secondary channels are computed separately by using Eq. 2.1 and Eq. 2.2 as defined by Beér and Chigier [15]. Swirl numbers are computed at the Venturi section with the same diameter of 30 mm.

$$SN_{pri} = \int_{0}^{R_{po}} \frac{U_{axial} \cdot U_{tangential} \cdot r^2 dr}{R_{po} \cdot U_{axial} \cdot U_{tangential} \cdot r dr} \tag{2.1}$$

$$SN_{sec} = \int_{R_{si}}^{R_{so}} \frac{U_{axial} \cdot U_{tangential} \cdot r^2 dr}{R_{po} \cdot U_{axial} \cdot U_{tangential} \cdot r dr} \tag{2.2}$$

It was suggested by Halpin [34] that the swirl number can be computed by taking the mass average of the primary and secondary swirl numbers. Eq. 2.3 is used to calculate the swirl numbers of all swirlers.

$$SN = \left| SN_{pri} \cdot \frac{\dot{m}_{pri}}{\dot{m}_{total}} \right| + \left| SN_{sec} \cdot \frac{\dot{m}_{sec}}{\dot{m}_{total}} \right| \tag{2.3}$$

Tab. 2.1 summarizes the geometrical properties of the swirlers. Additionally, to understand the effect of the introduction of flare geometry, experimental results obtained previously by Kıyıcı and Perçin [1] are compared with those of the present study. Geometrical parameters of this baseline swirler, which does not have a flare geometry, are also given in Tab. 2.1. Different flare configurations of the swirlers are demonstrated in Fig. 2.3.

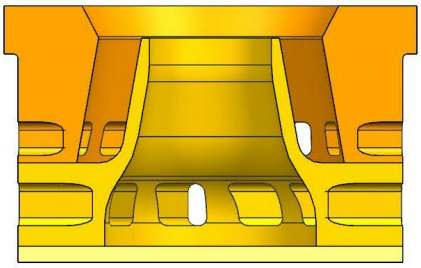
Table 2.1: Swirler geometrical properties

Name of the swirler	Sense of rotation	Swirl number	Flare geometry	Hydraulic diameter [mm]
27.5CH-CR	CR	1.2	27.5°Chamfer	30
45CH-CR	CR	1.2	45°Chamfer	30
Rad-CR	CR	1.2	Rounded (4 mm fillet)	30
Rad-CO	CO	1.2	Rounded (4 mm fillet)	30
Baseline[1]	CR	1.2	None	30

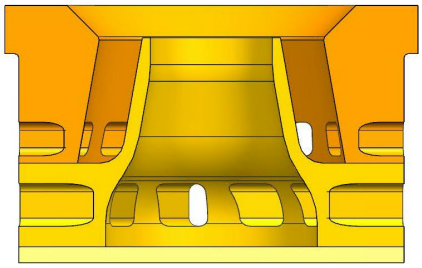
2.3 Experimental facility

The experiments were conducted on a non-reacting planar combustor rig test facility in RUZGEM - Center for Wind Energy of the Middle East Technical University. The planar non-reacting combustor rig is provided with high-pressure air with the use of compressors. A de-moisture system exists to extract the humidity from the air. The pressurized air travels through two pressure regulators which set the mass flow rate of the test section. The mass flow rate is checked using a Coriolis flow meter (the Micro Motion Coriolis F050S) before every run to assure that the test section mass flow rate of 12.9 g/s is achieved in all experiments. This mass flow rate sets the Reynolds number of the tests to a value of 35000 which is calculated at the swirler exit using values of the hydraulic diameter and the swirler exit velocity ($V_{exit} = 17.46 m/s$). A single-jet Laskin-type nozzle is used to atomize olive oil particles which are used as seeding material for the 2D2C PIV experiments. The seeding particles were atomized to an approximate diameter of 1 μm. Olive oil droplets mix with air inside the mixing chamber before entering the settling chamber. Inside the settling chamber, the air passes through a mesh screen so that uniform flow conditions are achieved before entering the test section. In previous studies conducted by Kıyıcı and Perçin [1], the conditions before the test section entrance were characterized by a set of PIV measurements at the settling chamber. The results obtained are tabulated in Tab. 2.2.

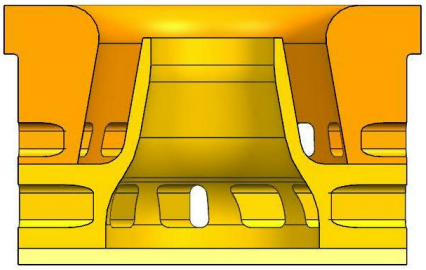
The radial-radial swirlers are placed between the settling chamber and the test section. The test section used for this study is of 120x120 mm^2 cross-section which provides a confinement ratio of 20.3. The confinement ratio is the ratio of the cross-section area of the flame tube to the cross-section area of the jet exit. The test section is made of



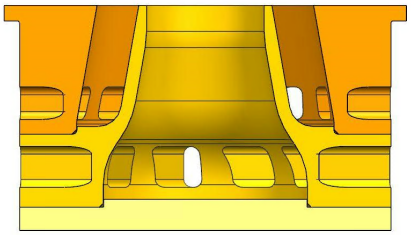
(a) Swirler with 27.5°flare



(b) Swirler with 45°flare



(c) Swirler with rounded flare



(d) Baseline swirler (w/o flare)

Figure 2.3: Swirler geometries

see-through Plexiglass for visual accessibility by the PIV equipment. The test facility is depicted with a schematic given in Fig. 2.4.

2.4 Particle image velocimetry test setup

Two-dimensional two-component PIV measurements are conducted on the swirler exit mid-plane. The velocity profile at the exit of the swirler is analyzed in order to determine its performance. The New Wave Research Solo 120 XT double pulse Nd:YAG laser, with a wavelength of 532 nm, is used to illuminate the tracer particles. Laser sheet optics are used in order to obtain a laser sheet thickness of approximately 1 mm at the measurement plane. A thin and properly aligned laser sheet is obtained as shown in Fig. 2.5 which prevents capturing and misinterpreting out-of-plane motions. The measurement plane is represented in Fig. 2.6. The laser pulses are separated by 60 μs in the time domain. The time spacing between the laser pulses is selected such that the motion of the tracer particles is restricted to be inside the interrogation windows. For conditions with higher flow speeds, a shorter time period between the

Table 2.2: Test section entrance properties [1]

Property	Value
Mean velocity at the exit of the settling chamber	0.89±0.1 $[m/s]$
Turbulence intensity at the exit of the settling chamber	8.9%
Uncertainty of mass flow rate provided to the test section	0.66%

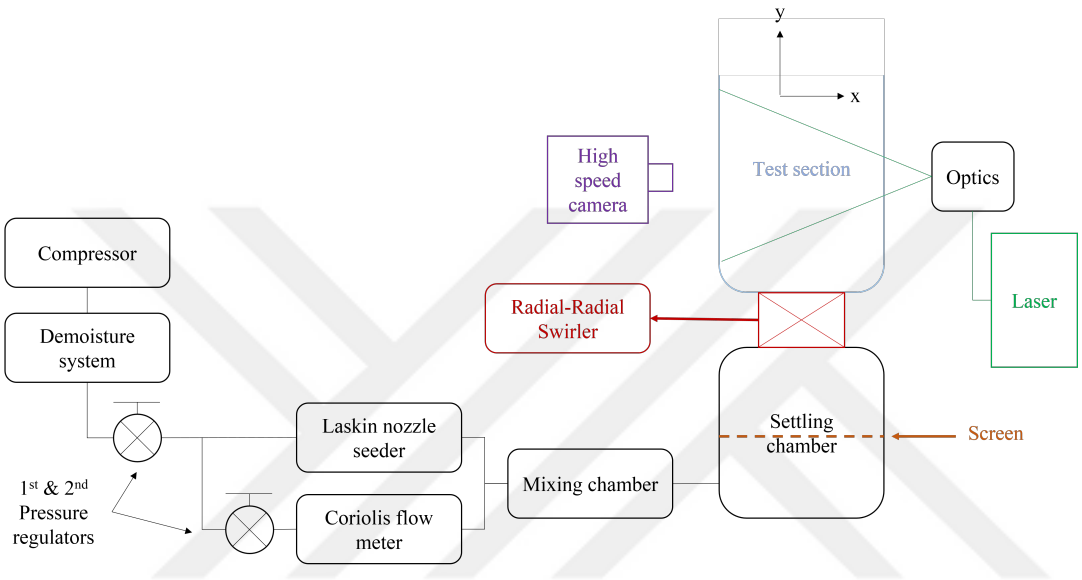


Figure 2.4: Experimental facility

laser pulses would be required. The field of view is calculated as $186.8 \times 116.8\ mm^2$ with a scale factor of 7.298 pixels/mm. However, the captured flow domain was narrowed due to excessive reflections and the $181 \times 111\ mm^2$ domain is evaluated.

To record the motion of the particles, the Phantom V641 high-speed camera (with a maximum resolution of 2560×1600 pixels^2 at 1500 fps) was utilized to shoot double-frame images synchronized with the laser pulses. It is aimed to obtain a statistically converged time-averaged flow field. Therefore, a total number of 2000 image pairs are recorded with a sampling rate of 20 Hz for each swirler geometry. Axial velocities at various distances from the swirler exit are checked to demonstrate statistical convergence of the mean flow field. The axial velocity values of the Rad-CR swirler at $y/D_h = 1$ distance from the swirler exit are presented in Fig. 2.7 for 10, 100, 1000

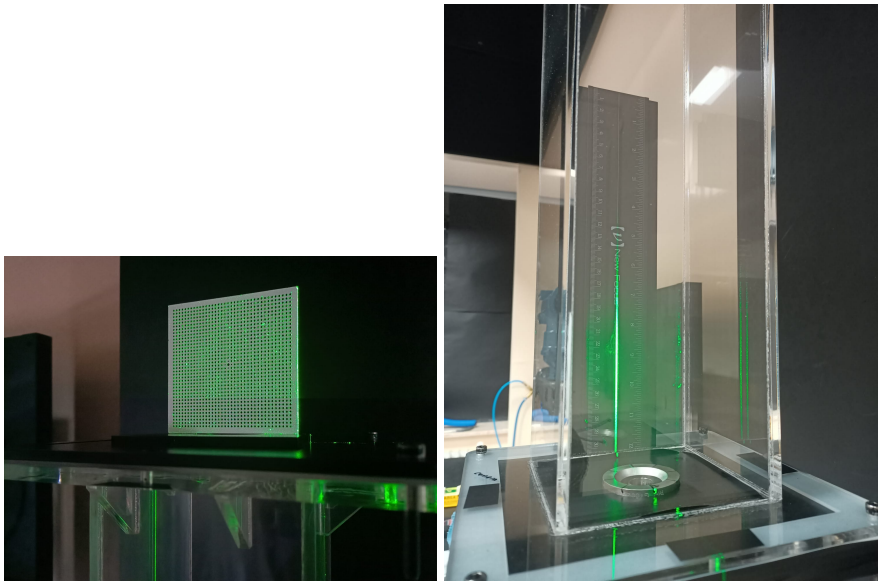


Figure 2.5: Thin and aligned laser sheet at mid-plane of the swirler exit

and 2000 image pairs.

The captured image pairs are post-processed via DANTEC Dynamic Studio v2015. The analysis sequence starts with the definition of regions of interest. The intention is to capture the flow field inside the confinement walls entirely. However, due to reflections, this is not achieved at near-wall regions. By defining the region of interest, the excessive reflection regions are removed from the images and are not included in the analysis. A low-pass filter is applied to the images for background subtraction. Next, an adaptive cross-correlation algorithm is used in order to obtain the velocity field in interrogation window sizes starting from 128x128 $pixel^2$ reducing to 32x32 $pixel^2$ in 2 steps. Universal outlier detection is used based on 3x3 cells, in order to remove erroneous velocity vectors which behave differently when compared to their neighboring vectors. The vector spacing in the 32x32 interrogation windows is given in Tab. 2.3 for the different swirler geometries. The first peak-to-second-peak ratio for the captured images is 4.46, which is used to assess the quality of the PIV images before continuing with the analysis. The value is considered to be satisfactory.

An image summarizing the test setup captured during the tests is given in Fig. 2.8.

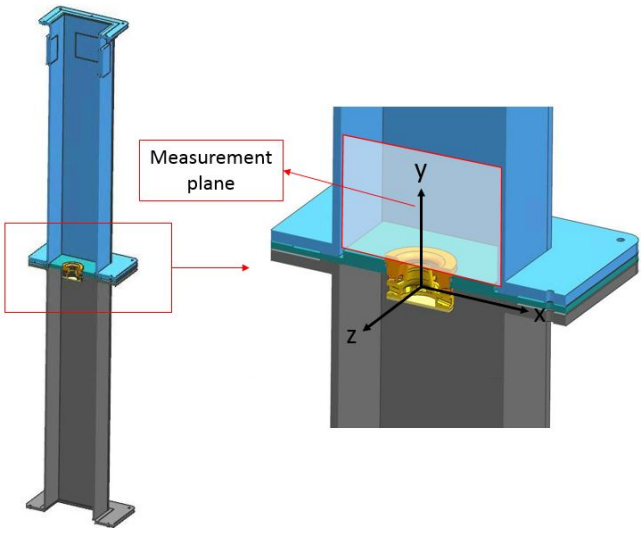


Figure 2.6: Swirler placements inside the test section and measurement plane

Table 2.3: Vector spacing of PIV images

Swirler geometry	Vector spacing $[mm]$
27.5CH-CR	1.23
45CH-CR	1.13
Rad-CR	1.07
Rad-CO	1.2
Baseline-CR [1]	1.1

2.5 Uncertainty analysis

To compute the statistical uncertainty values obtained for the first- and second-order moments the method suggested by Sciacchitano and Wieneke [35] is employed. The first-order moment uncertainties are computed using Eq. 2.4, whereas the second-order moment uncertainties are calculated with Eq. 2.5.

$$\delta_{\overline{U_i}} = Z_{\alpha/2}\sqrt{\frac{\overline{u_i^2}}{N}} \tag{2.4}$$

$$\delta_{\overline{u_i^2}} = Z_{\alpha/2}\sqrt{\frac{2\overline{u_i^2}^2}{N}} \tag{2.5}$$

The resulting uncertainties for a 95% confidence interval are tabulated via Tab. 2.4.

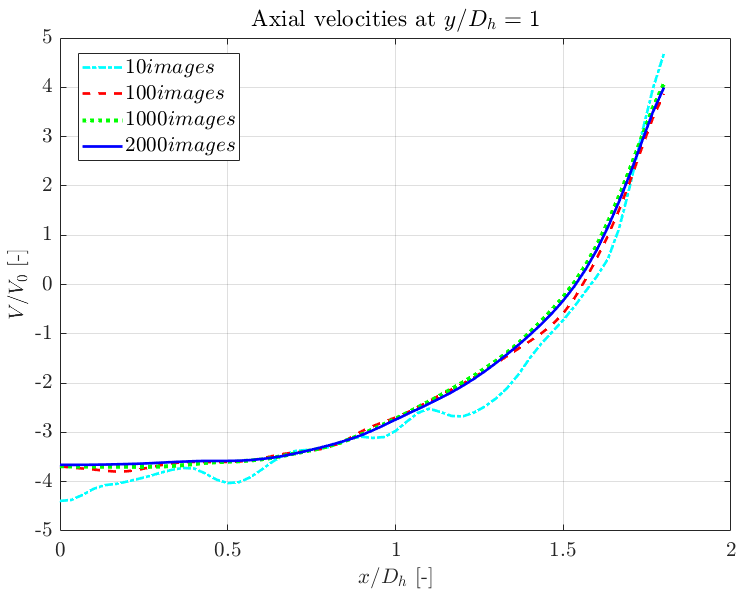


Figure 2.7: Axial velocity profiles of the Rad-CR swirler at $y/D_h = 1$ for 10, 100, 1000 and 2000 image pairs

Table 2.4: Statistical uncertainties in first- and second-order components for 95% confidence interval

	Component	Statistical Error (%)
First-order moments	Radial	0.533
	Axial	0.615
Second-order moments	TKE	2.609

2.6 Proper orthogonal decomposition

To identify the coherent structures of the swirling flow, several methods exist in literature. In this study, the snapshot proper orthogonal decomposition (POD) method is used [31]. First, Reynolds decomposition is applied to the flow, and properties are defined by mean and fluctuating properties as shown in Eq. 2.6.

$$V(x,t) = \overline{V}(x,t) + v'(x,t) \tag{2.6}$$

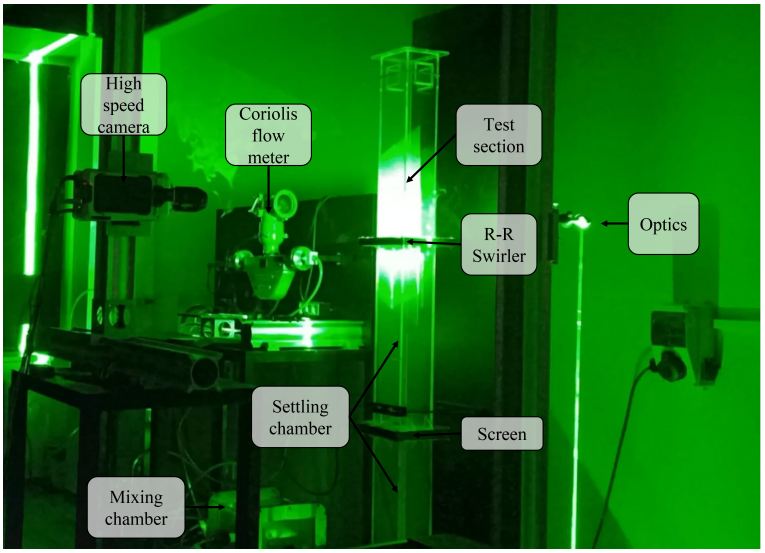


Figure 2.8: PIV Test Setup

The fluctuating part of the property can be defined as a series of temporal coefficients α, and spatial modes Ψ (Eq.2.7). Here, x and t are the space vector and time respectively, and N is the number of vector fields.

$$v'(x,t) = \sum_{i=1}^{N} \alpha_i(t) \cdot \Psi_i(x) \tag{2.7}$$

In order to obtain the temporal coefficients α_i, the eigenvalue problem needs to be solved by using the correlation matrix $C_{i,j}$ of size $N \times N$ given in Eq. 2.8.

$$C_{i,j} = \frac{1}{N} v'(x,t_i) T_{v'}(x,t_i) \tag{2.8}$$

The eigenvalues are ordered from largest to smallest in terms of their energy levels (Eq. 2.9) and the mode structures are obtained by the projection of snapshots onto the temporal coefficients as in Eq. 2.10.

$$C\alpha_i = \lambda_i \alpha_i \text{ and } \lambda_1 > \lambda_2 > \lambda_3 > ... > \lambda_N \tag{2.9}$$

$$\Psi_i(x) = \frac{1}{N\lambda_i} \sum_{i=1}^{N} \alpha_i(t_j) v'(x,t_j) \tag{2.10}$$

CHAPTER 3

RESULTS

In this section, the experimental results obtained by the 2D2C PIV measurements are provided. The effect of the introduction of flare expansion geometry, the change in the flow field due to the variation in flare geometry, and the impact of the channel orientation are investigated. The impact of the addition of the flare geometry is shown by comparison of test data for a baseline swirler obtained during previous studies by Kıyıcı and Perçin [1]. The effect of changing the flare geometry is shown by comparing three different flare configurations within themselves. Finally, the effect of channel orientation is investigated by comparing the CO and CR configurations of the flared swirlers.

All velocity magnitudes are non-dimensionalized with the swirler inlet velocity $V_0 = 0.89m/s$, while all lengths are non-dimensionalized with the hydraulic diameter of the swirler $D_h = 30mm$. The intention is to capture the entire flow field between the confinement walls extending from $x/D_h = +2$ to $x/D_h = -2$. However, due to the excessive reflection, this was not possible. Orange lines given in all contour plots in this section represent the flow domain boundaries. The green lines at $x/D_h = \pm 0.5$ represent the flare geometry of the swirler which has an extended surface above the test plate. No green line exists for the baseline swirler which is flush-mounted to the test plate. The white regions between the velocity contours and the green & orange lines are extracted regions due to excessive reflection.

The experimental results of the 2D2C PIV experiments are supported by 3D CFD results performed by Kıyıcı et. al. [36]. The CFD results are used to support the experimental data for two main reasons. Firstly, to obtain the change in the third velocity component which cannot be obtained by planar measurements. Second, to obtain data at the regions removed from the PIV images to improve image quality and

prevent distortion generated by excessive reflection. Details regarding the numerical method and setup used can be found in the work of Kıyıcı et. al. [36].

For the purpose of demonstration of the viability of the results obtained by the numerical analysis, the flow field obtained with the CFD simulations of the Rad-CR swirler is compared with the time-averaged flow field results obtained by 2D2C PIV experiments as shown in Fig. 3.1. Satisfactory agreement is obtained in terms of the flow topology. The width of the CTRZ shows similarity whereas it is not possible to compare the length of the CTRZ obtained from PIV and CFD since the CTRZ extends beyond the measurement plane captured by the PIV images. There are some discrepancies in the magnitude of the velocities. This can be better observed by looking at the axial velocity profiles.

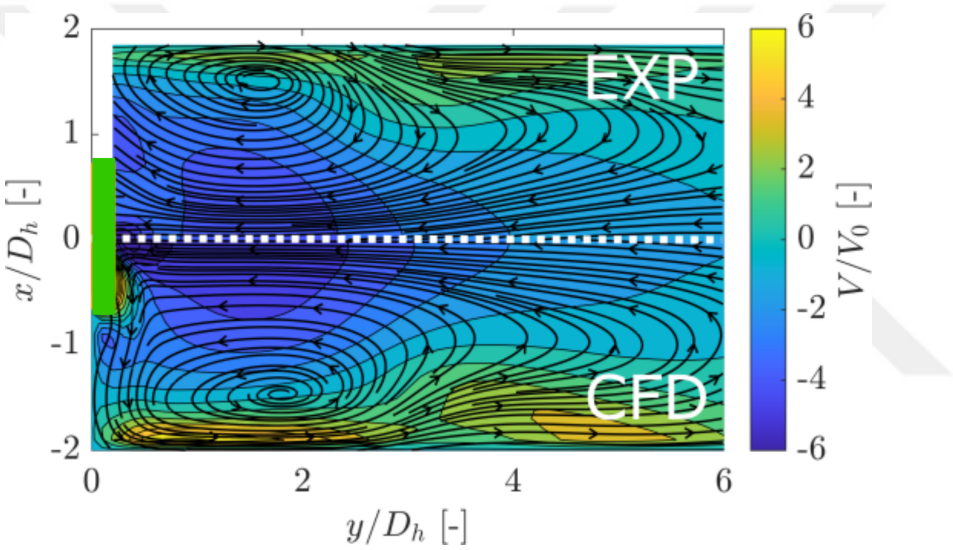


Figure 3.1: Direct comparison of experimental and numerical study data of the time-averaged flow field generated by the Rad-CR swirler

The axial velocity profiles obtained at $y/D_h = 1$ location for the Rad-CR swirler by CFD and by the 2D2C PIV measurements are compared in Fig.3.6. There are some differences between the axial velocities which may stem from the exit boundary condition definition and the deficit of the eddy-viscosity-based turbulence model dealing with highly-swirling flows [36]. The axial velocity disparity is along the centerline of the swirler and it increases as more downstream locations are investigated. The root-mean-square (RMS) of the axial velocities at $y/D_h = 1$ for the Rad-CR swirler obtained by CFD studies is found by Eq. 3.1 to be 0.412.

$$RMSE = \sqrt{\frac{\sum_{i=1}^{N}(x_i - \hat{x}_i)^2}{N}} \tag{3.1}$$

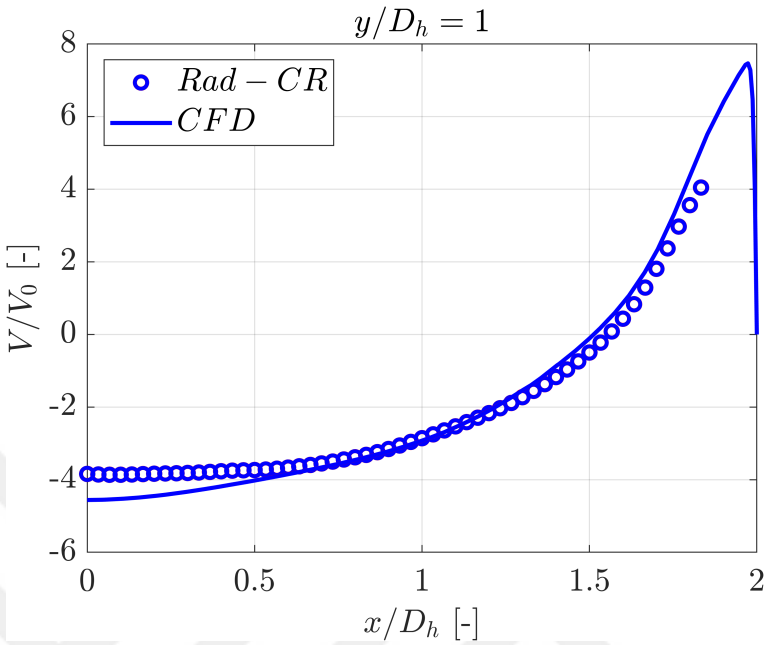


Figure 3.2: Comparison of axial velocity profiles obtained for the Rad-CR swirler at $y/D_h = 1$ via CFD and experiments

These CFD results will be used to draw some general conclusions rather than quantify any physical phenomena, thus the miscalculations are considered acceptable.

3.1 Effect of flare expansion

The effect of the addition of the flare geometry is studied by comparing the results obtained for the counter-rotating rounded flare radial-radial swirler (Rad-CR) with the flow field of a counter-rotating radial-radial swirler without a flare geometry (Baseline-CR) previously studied by Kıyıcı and Perçin [1]. The hydraulic diameters, swirl numbers, flow split, etc. are the same for both swirlers as pointed out in Sec. 2. The time-averaged flow field results are investigated in this section. The velocity profiles generated by Baseline-CR and Rad-CR swirlers are compared in Fig. 3.3.

For the Baseline-CR configuration, a high-speed swirling jet discharges from the swirler with an expansion angle of 35.62°[37]. This swirling jet attaches to the con-

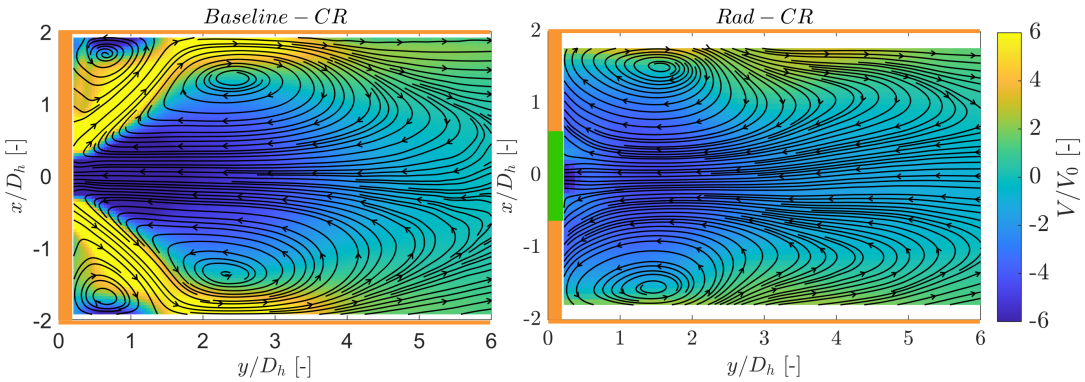


Figure 3.3: Time-averaged velocity fields in y-direction for Baseline-CR (left) and Rad-CR (right) swirlers

finement walls approximately 1.5 hydraulic diameters downstream of the swirler exit and continues to flow as a wall jet. Between the dome and the swirling jet, the formation of corner recirculation zone (CRZ) is observed. The work of Weigand et. al. [38] reveals that the region between the CRZ and the combustor dome can be subject to air temperatures of almost 80% of the maximum air temperature encountered during combustion. The corner recirculation zone generates a region of high-temperature gases trapped close to the combustor dome.

Moreover, a central toroidal recirculation zone (CTRZ) is formed that extends to more than 6 hydraulic diameters. Although the length of the CTRZ is beyond the extent of the PIV images, it can be predicted from the shown data that the CTRZ of the Baseline-CR configuration is about to close. Shorter and more compact CTRZ regions are more desirable for flame stabilization due to the prevention of the recirculation of cold flow in a long CTRZ [14]. In some cases, it was found that the combustion process was already completed before the closure of the CTRZ lowering the combustion efficiency as well as blow-off limits. Large values for positive velocities are obtained at the swirling jet whereas negative peaks are observed at the CTRZ penetrating into the swirler exit. For the Rad-CR swirler, the axial velocity component at the swirler exit becomes smaller, and the radial velocity component magnitude increases. Thus, the swirling jet directly attaches to the dome and keeps moving downstream as a wall jet. The formation of a wide CTRZ is observed whereas the CRZ does not form. The CTRZ extends beyond the measurement plane. In literature, the flow topology of the Baseline-CR is termed as a typical conical form

vortex breakdown flow structure [11], while the flow structure of the Rad-CR swirler is termed as a wide-open conical form of vortex breakdown flow structure [39].

According to the results obtained by Estefanos [25], [27], swirlers with and without flare were found to behave differently when compared to the current study. They stated that the same swirler without flare geometry had a wider expansion of the swirling jet and the flare restricts the expansion of the swirling jet. Comparison with this study signifies the dominance of the confinement ratio and the swirl number on the jet expansion.

The normalized turbulence kinetic energy contours of the Baseline-CR and the Rad-CR swirlers are given in Fig. 3.4. It is important to note that the TKE is calculated as given in Eq. 3.2 since only two components of velocity are obtained via planar PIV measurements.

$$TKE = \frac{1}{2}(\overline{(u')^2} + \overline{(v')^2}) \tag{3.2}$$

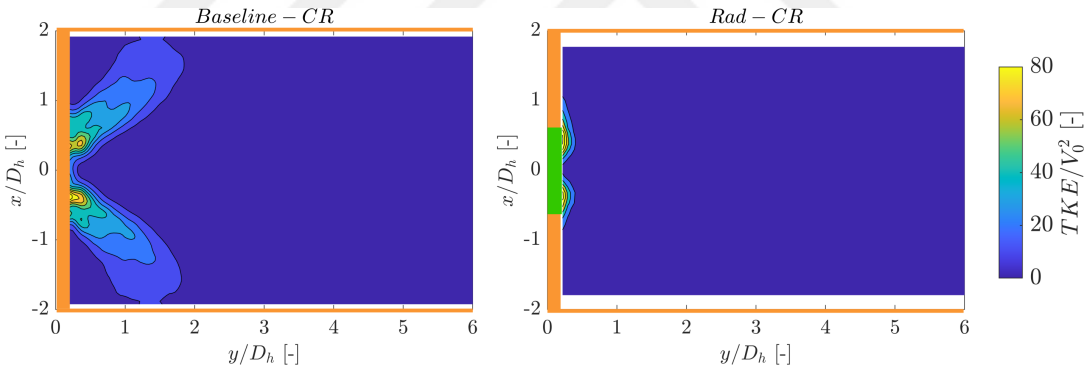


Figure 3.4: Normalized TKE ratio contour of Baseline-CR (left) and Rad-CR (right) swirlers

The TKE contours reveal high turbulence intensity regions of the flow field which are usually associated with shear layers. Higher levels of TKE for the Baseline-CR swirler are observed at the swirling jet region. Intense mixing of cold and fresh gas with hot and burned gas coming from the CTRZ is expected in the high TKE region [38]. The regions where the swirling jet-CTRZ interaction and the swirling jet-CRZ interaction occur, are regions with high turbulence intensity for the Baseline-CR. However, for the Rad-CR configuration, due to the rapid expansion of the swirling

jet highly turbulent regions are directly at the swirler exit and the intensity decays rapidly as the flow moves downstream. From the time-averaged velocity fields and the TKE contours, it can be clearly seen that a small in change swirler geometry has a dramatic impact on the flow field generated by radial-radial swirlers.
Further investigation on the velocity field was conducted by extracting the axial and radial velocity components at 0.5, 1 and 2 hydraulic diameters downstream of the swirler exit. The results are represented in Fig. 3.5. In this figure, $x/D_h = 0$ corresponds to the exit of the swirler, and only one-half of the measurements plane is shown. Starting with the axial velocities, it is observed that there is a strong axial negative velocity penetrating into the center of the Baseline-CR swirler. In reactive conditions, this might contribute to the transportation of the hot combustion products from the CTRZ to the venturi section as was observed by Weingand [38]. At further downstream locations, the magnitude of the peak negative axial velocity keeps decreasing. The CTRZ of the Baseline-CR swirler widens from $x/D_h = 0.38$ to $x/D_h = 1.31$ when moving from $y/D_h = 0.5$ to $y/D_h = 2$, but is always narrower when compared to the CTRZ width of the Rad-CR. The change in the axial velocity profile of the Rad-CR swirler with increasing distance from the swirler exit is not as remarkable. Peak positive axial velocities seem to be occurring at near-wall regions. The data obtained by CFD shown in Fig. 3.6 is used to depict the velocity at near-wall regions which had to be removed from the PIV images due to intensive reflection. For the Rad-CR swirler, the flow attaches to the dome very close to the swirler exit, the CTRZ is already developed at $y/D_h = 0.5$, and the values of the axial velocities as well as the extent of the CTRZ do not change significantly when moving downstream. The formation of the CRZ is observed for the Baseline-CR case, revealing itself from the negative axial velocity values at $y/D_h = 0.5 - 1$. The CRZ diminishes when the swirling jet attaches to the wall and is not observed at $y/D_h = 0.5 - 1$.

The radial velocities of the Baseline-CR swirler have large magnitudes at the swirling jet regions before the jet attaches to the wall. The positive peak value moves toward the wall which once again depicts the widening of the CTRZ. Negative values of the radial velocity are observed at the center of the swirler exit and around the "eye" of the CRZ at $y/D_h = 0.5$ for the Baseline-CR. For the Rad-Cr swirler at $y/D_h = 2$ all radial velocity values are negative and flow recirculates around the "eye" of the

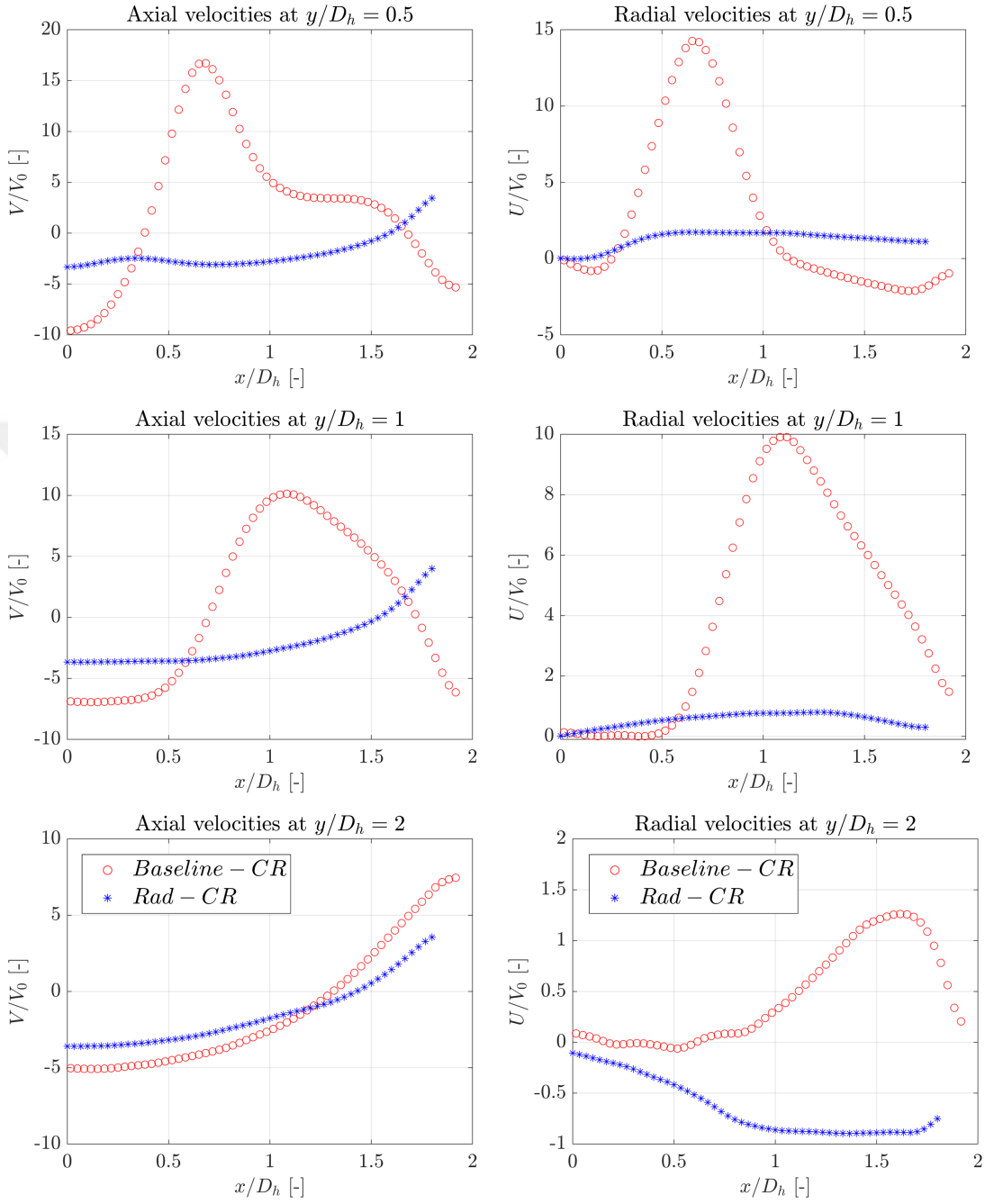
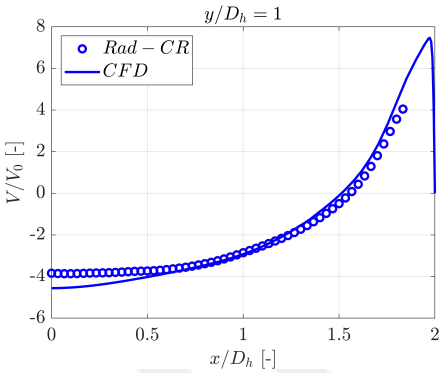
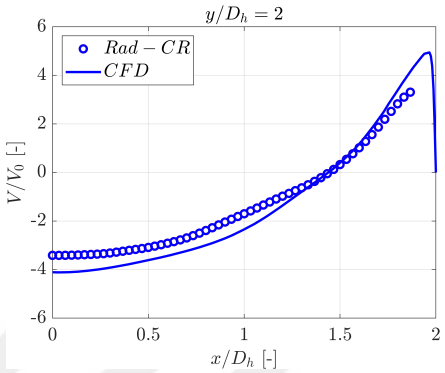


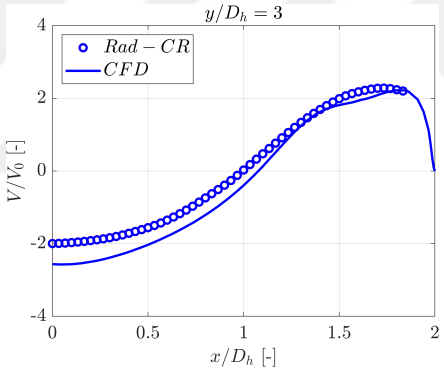
Figure 3.5: Time-averaged axial and radial velocity components at $y/D_h = 0.5, 1\&2$ of the Baseline-CR and Rad-CR swirlers



(a) Axial velocity profiles of the Rad-CR swirler at $y/D_h = 1$



(b) Axial velocity profiles of the Rad-CR swirler at $y/D_h = 2$



(c) Axial velocity profiles of the Rad-CR swirler at $y/D_h = 3$

Figure 3.6: Comparison of axial velocity profiles obtained for the Rad-CR swirler via CFD and experiments at various streamwise locations

CTRZ. The radial expansion of the Rad-CR swirler is completed at locations close to the swirler exit. Therefore, the positive values of radial velocity are not as high in magnitude as the Baseline-CR configuration for which the radial expansion is not completed up to $y/D_h \cong 1.5$.

In order for a better understanding of the velocity fields, numerical results are used to support the experimentally obtained data. Fig. 3.7 shows the axial pressure gradients at the symmetry axis of the Baseline-CR and Rad-CR configurations. Much stronger adverse pressure gradients are obtained at $y/D_h = 1$ for the Baseline-CR which is the reason behind the difference in the axial velocity magnitudes at the swirler exit.

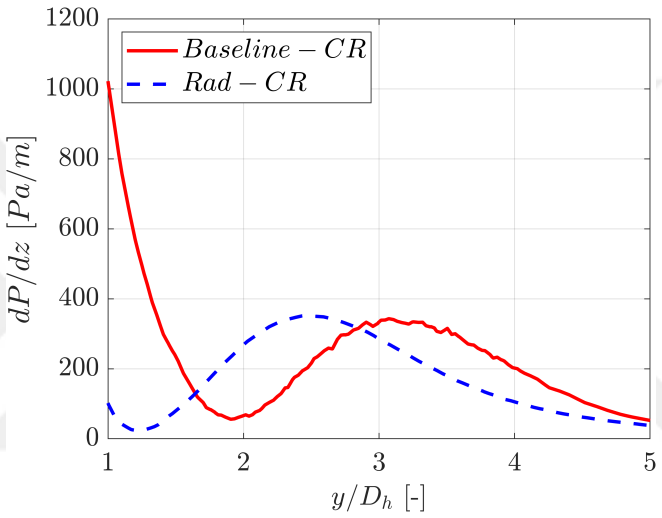


Figure 3.7: Numerical results of axial pressure gradients at the symmetry axis of the Baseline-CR and Rad-CR swirlers

The velocity components at the flare exit are extracted from numerical results and shown in Fig. 3.8. With the help of these velocity profiles, the swirl number at the flare exit is calculated to be 0.4. Under reactive conditions, the swirl number can decrease even further due to axial acceleration with the combustion progress [38]. From the venturi section to the flare exit, the primary and secondary flows interact with each other and have a dampening effect on the swirl numbers. Although the swirl number is decreased, vortex breakdown still occurs due to the geometry of the flare. The flow expands rapidly with a high radial velocity. Higher swirl numbers are found to increase flame stability, especially in the rich extinction region [14]. With a higher swirl, the rich extinction limit is shifted to a lower mixture ratio which helps

the flame to be insensitive to random variations in mixture ratio.

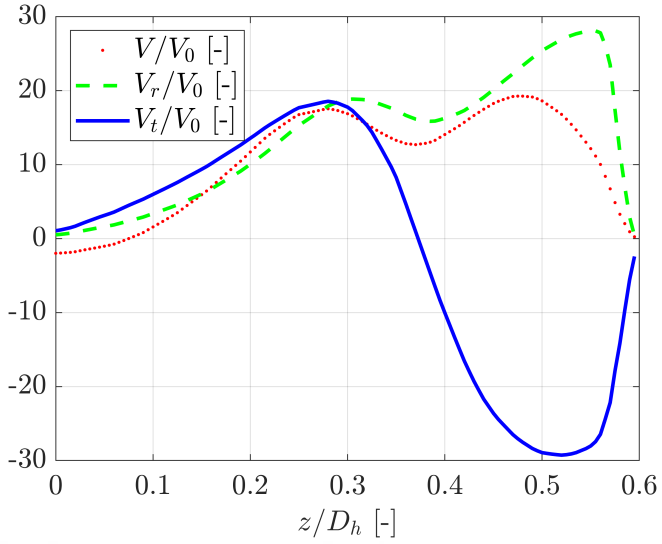


Figure 3.8: Numerical results of velocity components at flare exit of the Rad-CR swirler

3.2 Effect of flare geometry

The effect of the flare geometry was investigated by comparing the flow fields generated by three flare geometries with two different expansion angles, and one with a rounded shape. The time-averaged flow fields are shown in Fig. 3.9. Almost identical flow structures are obtained with wide recirculation zones. The formation of the CRZ is not observed in any flare geometry. Velocity magnitudes at the CTRZ are similar.

Next, the normalized TKE of the different flare geometries are compared in Fig. 3.10. Characteristics seem to be similar at first glance. The normalized TKE for the Rad-CR levels at the swirler exit are larger when compared to the chamfered geometries. The high turbulent regions extend to more than 1 hydraulic diameter radially for the chamfered geometries. However, for all geometries, the TKE is significant at the swirler exit and diminishes immediately.

In order to understand the similarity of the flow fields, the axial and radial velocity components are compared at $y/D_h = 0.5, 1\&2$ location as shown in Fig. 3.10. The axial velocities are almost identical, especially at the CTRZ region. Only at the near-

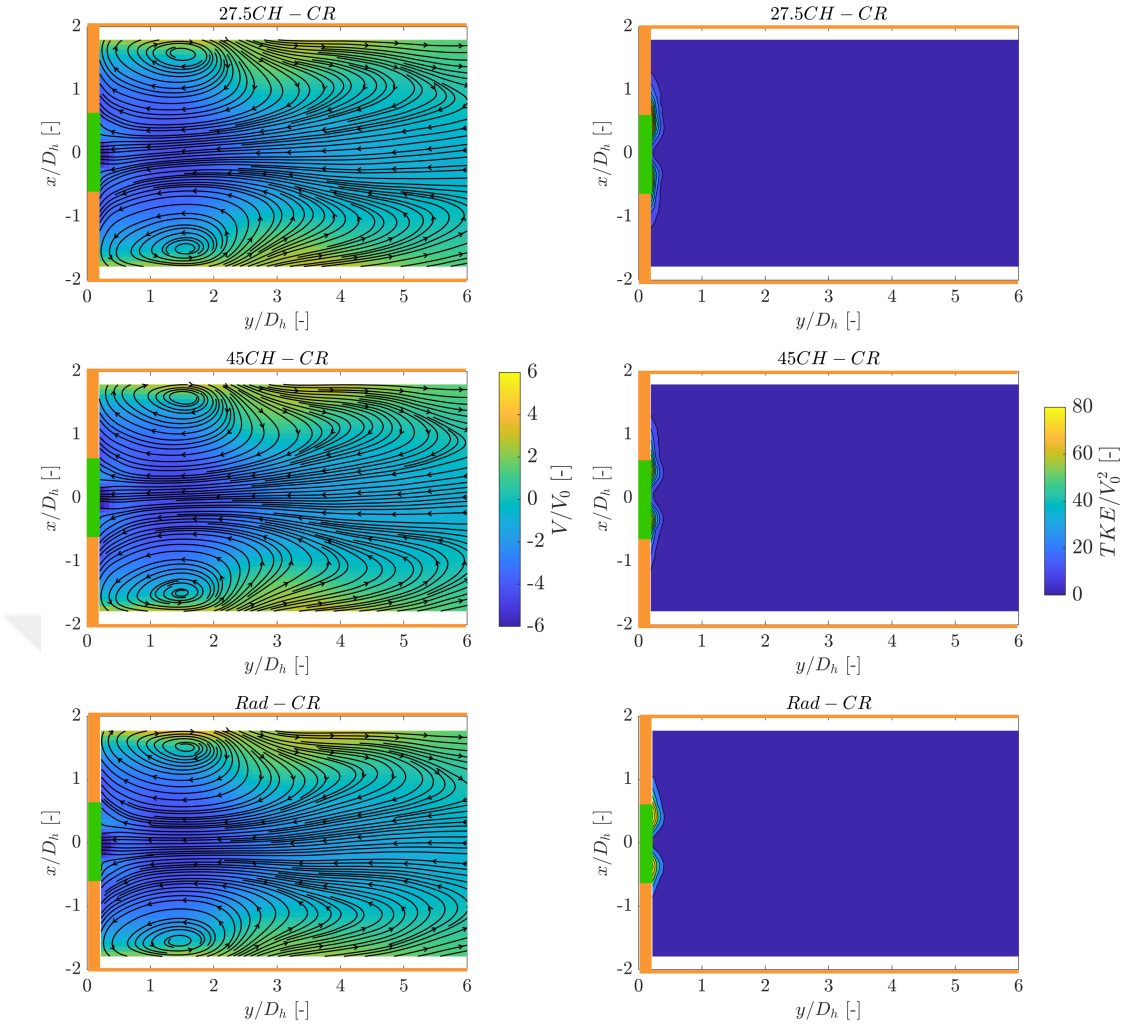


Figure 3.9: Time-averaged velocity fields in y-direction for 27.5CH-CR, 45CH-CR, and Rad-CR swirlers

wall regions with positive axial velocities, do the values of axial velocities vary by a small amount. The radial velocities however show different characteristics as the flare geometry is varied. However, due to the low values of the radial velocities, a significant observation of the change in radial velocity with the flare geometry can not be made. Largest values of the radial velocity are observed at the swirler exit. The recirculating mass flow rate values and the width of the CTRZ are computed and compared. The width of the recirculation zone is defined as the distance between the "eye"s of the recirculation zones. This definition is used as suggested by Kıyıcı and Perçin [1]. To calculate the recirculating mass flow rate, Eq. 3.3 is used. The results are normalized with the recirculating mass flow rate of the Baseline-CR and given

in Tab. 3.1. From the tabulated values, it is shown that the recirculating mass flow rate increases with the addition of the flare geometry. This stems from the increase in the width of the CTRZ, despite the decrease in the axial velocity of the recirculating mass flow. Moreover, as the flare geometry changes, the same width of the CTRZ is obtained with a slight change in recirculating mass flow rate values.

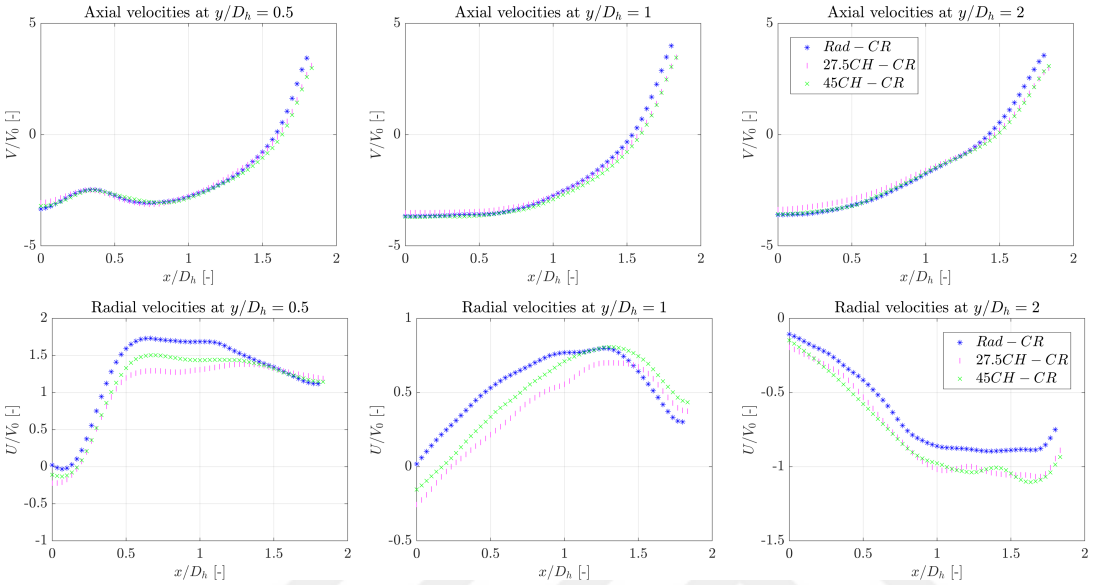


Figure 3.10: Time-averaged axial and radial velocity components at $y/D_h = 0.5, 1\&2$ of the 27.5CH-CR, 45CH-CR, and Rad-CR swirlers

$$\dot{m}_{recirculating} = 2 \cdot \pi \cdot \rho \int_0^R r \cdot V_{axial} \cdot dr \tag{3.3}$$

Table 3.1: Normalized recirculating mass flow rate and CTRZ width values of various swirler geometries

Case	Normalized $\dot{m}_{recirculating}$	R/D_h
Baseline-CR	1.000	1.333
Rad-CR	1.233	1.467
CH27.5-CR	1.102	1.467
CH45-CR	1.127	1.467
Rad-CO	1.556	1.467

Considering the information given in this section, it is concluded that for the investigated confinement ratio and swirl number, the flare geometry does not significantly

influence the flow field generated by radial-radial swirlers. The axial velocities, TKE levels, recirculation widths, etc. show great similarity. Comparison with the work of Estefanos [25] reveals that the radial expansion of the swirling jet with increasing flare expansion angle would be observable for lower confinement ratios.

3.3 Effect of channel orientation

To comprehend the effect of the channel orientation, the rounded flare was tested in both, co- and counter-rotating configurations. The time-averaged velocity field in the y-direction is shown in Fig. 3.11. From the velocity contours, it is seen that for the co-rotating configuration, the CTRZ penetrates into the swirler with higher negative axial velocity values. The co-rotating primary and secondary jet flows interact with each other which causes an increase in the tangential momentum and velocity.

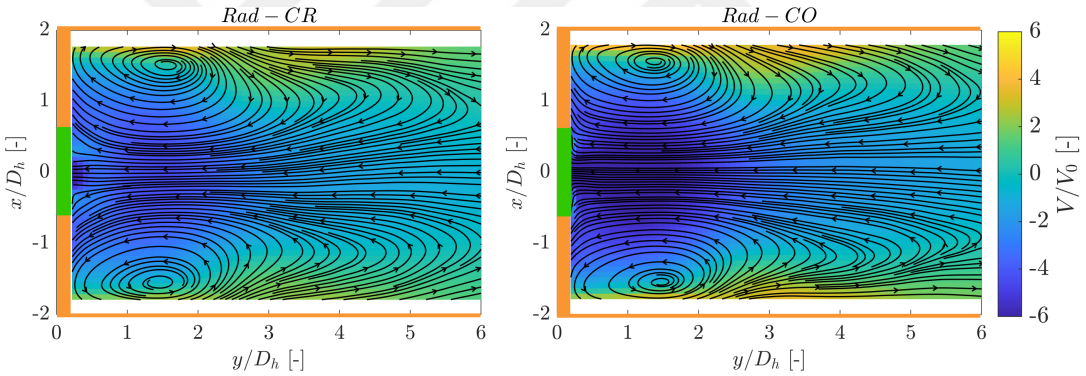


Figure 3.11: Time-averaged velocity fields in y-direction for Rad-CR (left), Rad-CO (right) swirlers

The normalized TKE contours of the Rad-CR and Rad-CO swirlers are shown in Fig. 3.12. The intensity of the turbulence is much greater for the Rad-CO case hence the larger TKE values. In addition, the radial extent of the high TKE regions is much larger for the Rad-CO geometry. The interaction between the primary and secondary channels generates a shear layer resulting in higher dissipation. In both cases, the swirling jet expands immediately after leaving the swirler exit and attaches to the wall. An increase in the width of the recirculation zone is not observed although the recirculating mass flow rate increases for the co-rotating case as given in Tab.

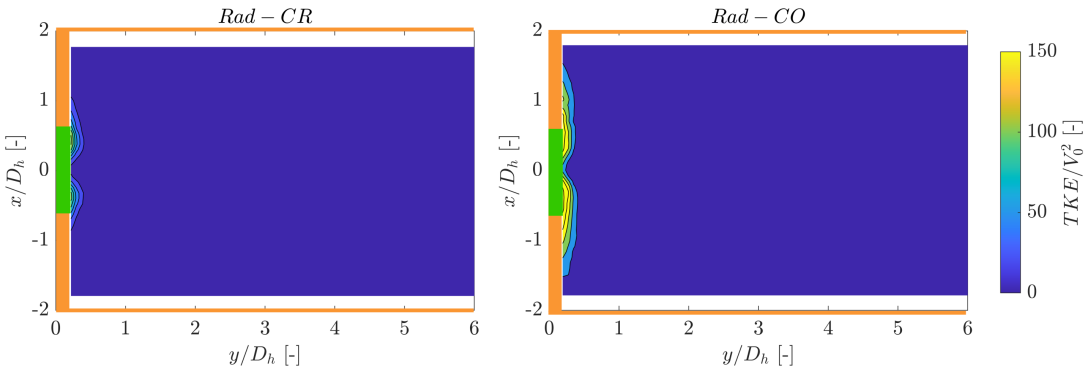


Figure 3.12: Normalized TKE ratio contour of Rad-CR (left), Rad-CO (right) swirlers

3.1. The reason for this is the stronger axial pressure gradient resulting in higher reverse flow velocities. In order to show this, the axial velocity values are plotted at $y/D_h = 0.5, 1\&2$ for both cases in Fig. 3.13.

3.4 POD results

A snapshot POD analysis is conducted on the fluctuating velocity components of all swirler geometries investigated within this study. The normalized kinetic energy content of the first twenty modes is given in Fig. 3.14. 50% of the total kinetic energy is contained in the first 35 modes for all swirler configurations. It is shown that 9-13% of the total kinetic energy content is captured by the first two modes. This value is rather low showing that highly dominant coherent structures do not exist in this case. This might be due to the presence of incoherent structures in the flow of interest.

Fig. 3.15 depicts the first five modes in terms of contours of axial velocities of the Baseline-CR, Rad-CR, and Rad-CO swirlers in descending order. It is observed that the most energetic modes are located near the confinement wall region for Rad-CR and Rad-CO swirlers. The sudden expansion of the swirling jet and it becoming a wall jet leads to the energetic coherent modes near the vicinity of the confinement walls. For the Baseline-CR swirler however, the most energetic coherent modes exist near the swirling jet. For the Rad-CR swirler, the first two modes are linked with the radial expansion & contraction of the CTRZ. In the work of Weigand [38], it was observed that the periodic changes in the expansion/contraction motion of the CTRZ

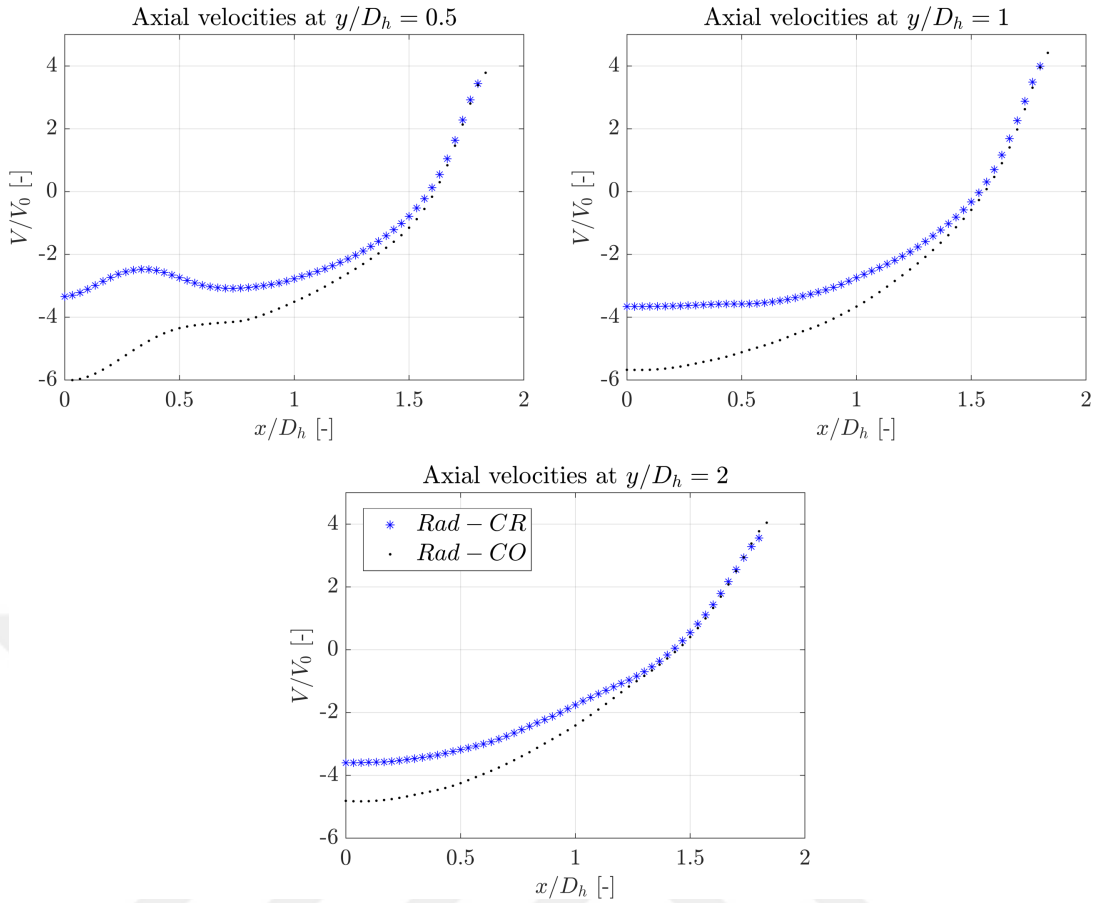


Figure 3.13: Time-averaged axial velocity components at $y/D_h = 0.5, 1\&2$ of the Rad-CR and Rad-CO swirlers

and CRZ enhanced the mixing of fuel, air, and exhaust gas which contributes to the increased reaction progress. The next two modes in descending energy content are identified as the distortion of the recirculation zone. The fifth and final mode included in this study represents the lateral swinging motion of the recirculation region. The remaining coherent modes and flow structures related to them show great resemblance to the five which are presented, hence they are not included here. When the Rad-CO and Rad-CR modes are compared with each other, it is seen that the modes are similar in shape and opposite in direction. For the Baseline-CR, symmetric and anti-symmetric structures are obtained. The precessing vortex core reveals itself over a range of modes. The anti-symmetric structure of the third most energetic mode is similar to the precessing vortex core flow pattern obtained by Sieber et. al. [11].

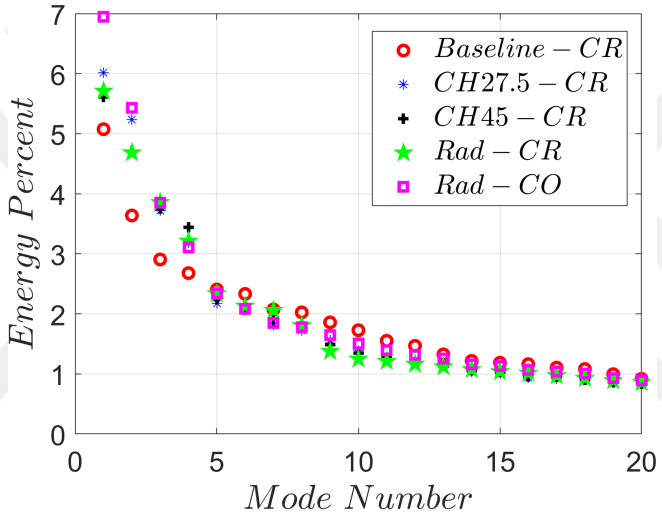


Figure 3.14: Energy modes for different flare geometries

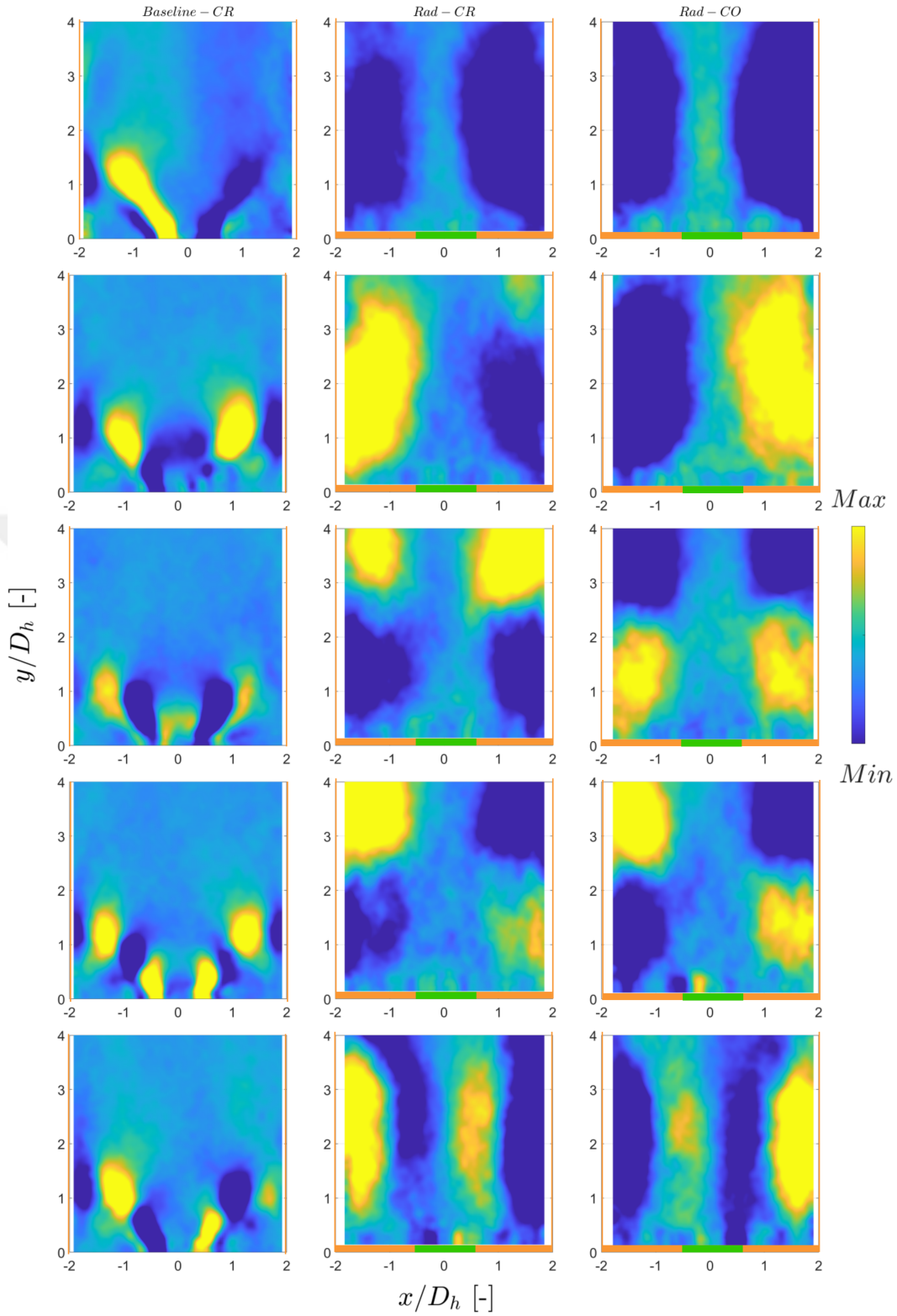


Figure 3.15: Representation of the first five POD modes in descending order by means of contours of the velocity component in the y-direction for the Baseline-CR (left), Rad-CR (middle), and Rad-CO (right) swirlers

CHAPTER 4

CONCLUSIONS

In this thesis, an experimental study on the effect of the flare geometry on the flow field generated by radial-radial swirlers is investigated. The results of a 3D numerical analysis are used to support the data obtained by 2D2C PIV measurements. In total, four different swirler geometries with flare expansion and one baseline geometry without a flare are investigated.

First, the time-averaged flow fields of the Baseline-CR and the Rad-CR are compared to understand the impact of the added flare expansion geometry. Results reveal a significantly changed flow field converting the typical conical form of vortex breakdown obtained for the Baseline-CR, to a wide-open conical form of vortex breakdown with the only changing parameter being the flare expansion geometry. The introduction of the flare, caused the swirling jet to expand rapidly, attach to the dome and move along the confinement walls as a wall jet. The formation of the CRZ was not observed for the Rad-CR configuration. In literature, it was observed that the CRZ region is a relatively high-temperature region which makes the elimination of this region an important aspect related to the combustor design. A wider and longer CTRZ is observed encompassing lower peak values of the negative axial velocity for the Rad-CR configuration. However, in terms of flame stability, a shorter and more compact CTRZ is more preferable. The CFD results show very strong adverse pressure gradients generated by the Baseline-CR swirler, shedding light on the reason for the higher negative axial velocity in the CTRZ penetrating into the swirler. High turbulence regions are located right at the swirler exit for the swirler geometries employing a flare whereas, for the baseline swirler, the most intense regions in terms of turbulence are obtained at shear layers between the swirling jet-CTRZ and the swirling jet-CRZ interaction regions. Regions of high TKE are regions of intense mixing which is important for

the combustion process.

Three different flare geometries are compared: 27.5°, 45°chamfered flares, and a filleted flare with a radius of 4 mm. For the design swirl number of 1.2 and the confinement ratio of 20.3 in this study, the flare geometry seems not to have a significant impact on the flow topology generated by the swirler. The width of the CTRZ and mass flow rates recirculating are obtained to be very similar.

The impact of the channel rotation was explored by comparing the flow fields of the Rad-CO and Rad-CR configurations. The interaction between the primary and secondary jets of the Rad-CO led to higher tangential momentum. When angular momentum conservation is applied, higher adverse axial pressure gradients are observed for the Rad-CO provided that similar lateral sizes of the CTRZ are obtained. Thus, larger values of negative axial velocities are penetrating into the swirler exit.

Finally, the snapshot POD method is employed on the fluctuating velocity component to obtain the energetic modes and identify coherent flow structures for the Baseline-CR, Rad-CR, and Rad-CO configurations. Modes obtained for co- and counter-rotating swirlers with the same flare geometry are obtained to be identical with opposite signs. Modes related to the expansion/contraction, distortion, and lateral swinging motion of the CTRZ generate the most energetic five modes for the geometries with flare. The analogy between the POD results of the Baseline-CR obtained within this study, and the POD and SPOD results found in the literature reveals signs of PVC presence among a range of modes of the Baseline-CR swirler.

REFERENCES

[1] F. Kıyıcı and M. Perçin, "Experimental investigation of the confinement effects in radial-radial swirlers," in *Turbo Expo: Power for Land, Sea, and Air*, vol. 84942, p. V03AT04A010, American Society of Mechanical Engineers, 2021.

[2] P. P. Walsh and P. Fletcher, *Gas turbine performance*. John Wiley & Sons, 2004.

[3] S. Farokhi, *Aircraft propulsion*. John Wiley & Sons, 2014.

[4] A. Andreini, R. Becchi, B. Facchini, A. Picchi, and A. Peschiulli, "The effect of effusion holes inclination angle on the adiabatic film cooling effectiveness in a three-sector gas turbine combustor rig with a realistic swirling flow," *International Journal of Thermal Sciences*, vol. 121, pp. 75–88, 2017.

[5] A. H. Lefebvre and D. R. Ballal, *Gas turbine combustion: alternative fuels and emissions*. CRC press, 2010.

[6] Y.-H. Kao, S. B. Tambe, and S.-M. Jeng, "Effect of chamber length with converging exhaust on swirling flow field characteristics of a counter-rotating radial-radial swirler," in *Volume 1B: Combustion, Fuels and Emissions*, American Society of Mechanical Engineers, June 2013.

[7] C. Çıray, *Akışkanlar Mekaniğine Giriş Üçüncü Kitap: Türbülans ve Bazı Türbülanslı Akımlar*. ODTÜ Yayıncılık, 1 ed., Ocak 2013.

[8] N. Sinha, *Towards RANS Parameterization of Vertical Mixing by Langmuir Turbulence in Shallow Coastal Shelves*. University of South Florida, 2013.

[9] K. Taira, S. L. Brunton, S. T. Dawson, C. W. Rowley, T. Colonius, B. J. McKeon, O. T. Schmidt, S. Gordeyev, V. Theofilis, and L. S. Ukeiley, "Modal analysis of fluid flows: An overview," *Aiaa Journal*, vol. 55, no. 12, pp. 4013–4041, 2017.

[10] N. Syred, "A review of oscillation mechanisms and the role of the precessing vortex core (pvc) in swirl combustion systems," *Progress in Energy and Combustion Science*, vol. 32, no. 2, pp. 93–161, 2006.

[11] M. Sieber, C. Oliver Paschereit, and K. Oberleithner, "Advanced identification of coherent structures in swirl-stabilized combustors," *Journal of Engineering for Gas Turbines and Power*, vol. 139, no. 2, 2017.

[12] K. Oberleithner, M. Stöhr, S. H. Im, C. M. Arndt, and A. M. Steinberg, "Formation and flame-induced suppression of the precessing vortex core in a swirl combustor: experiments and linear stability analysis," *Combustion and Flame*, vol. 162, no. 8, pp. 3100–3114, 2015.

[13] M. Raffel, C. E. Willert, J. Kompenhans, *et al.*, *Particle image velocimetry: a practical guide*, vol. 2. Springer, 1998.

[14] N. Syred and J. Beér, "Combustion in swirling flows: A review," *Combustion and Flame*, vol. 23, pp. 143–201, Oct. 1974.

[15] J. Beér and N. Chigier, *Combustion Aerodynamics*. Fuel and energy science series, Krieger, 1983.

[16] Y.-H. Kao, J. B. Haseman, S. B. Tambe, and S.-M. Jeng, "Aerodynamics comparisons between two typical gas turbine combustion swirlers," in *Volume 4B: Combustion, Fuels and Emissions*, American Society of Mechanical Engineers, June 2014.

[17] K. Merkle, H. Haessler, H. Büchner, and N. Zarzalis, "Effect of co-and counter-swirl on the isothermal flow-and mixture-field of an airblast atomizer nozzle," *International Journal of Heat and Fluid Flow*, vol. 24, no. 4, pp. 529–537, 2003.

[18] E. Kilik, "A numerical study of co-and counter-swirling confined coaxial jets," in *22nd Joint Propulsion Conference*, p. 1722, 1986.

[19] Y. Fu, J. Cai, S.-M. Jeng, and H. Mongia, "Confinement effects on the swirling flow of a counter-rotating swirl cup," in *Turbo Expo: Power for Land, Sea, and Air*, vol. 4725, pp. 469–478, 2005.

[20] Y. Fu, J. Cai, S.-M. Jeng, and H. Mongia, "Characteristics of the swirling flow generated by a counter-rotating swirler," in *43rd AIAA/ASME/SAE/ASEE Joint Propulsion Conference & Exhibit*, p. 5690, 2007.

[21] F. K. Battal Gencer and M. Perçin, "Effects of vane numbers/types on the swirling flow field characteristics of a counter-rotating radial-radial swirler," in *AIAC2021*, AIAC2021, Sept. 2021.

[22] K. Merkle, H. Bu¨chner, N. Zarzalis, and O. N. Sara, "Influence of co and counter swirl on lean stability limits of an airblast nozzle," in *Volume 2: Turbo Expo 2003*, ASMEDC, Jan. 2003.

[23] S. Marinov, M. Kern, K. Merkle, N. Zarzalis, A. Peschiulli, F. Turrini, and O. N. Sara, "On swirl stabilized flame characteristics near the weak extinction limit," in *Volume 2: Combustion, Fuels and Emissions, Parts A and B*, ASMEDC, Oct. 2010.

[24] J. Cai, F. Ichihashi, B. Mohammad, S. Tambe, Y.-H. Kao, and S.-M. Jeng, "Gas turbine single annular combustor sector: Combustion dynamics," in *48th AIAA Aerospace Sciences Meeting Including the New Horizons Forum and Aerospace Exposition*, American Institute of Aeronautics and Astronautics, Jan. 2010.

[25] W. Estefanos, S. Tambe, and S.-M. Jeng, "Effect of the flare expansion angle on the mean and dynamic behavior of swirling flow generated by a counter rotating radial-radial swirler using a water test rig," in *Turbo Expo: Power for Land, Sea, and Air*, vol. 56697, p. V04BT04A035, American Society of Mechanical Engineers, 2015.

[26] J. Brennan, *Experimental Investigation of Chevrons in Radial-Radial Swirlers*. PhD thesis, University of Cincinnati, 2013.

[27] W. Estefanos, S. Tambe, and S.-M. Jeng, "A study of the mean and dynamic behavior of the swirling flow generated by a counter rotating radial-radial swirler using a water test rig," in *Turbo Expo: Power for Land, Sea, and Air*, vol. 56697, p. V04BT04A033, American Society of Mechanical Engineers, 2015.

[28] H. Y. Wang, V. G. McDonell, and S. Samuelsen, "Influence of hardware design

on the flow field structures and the patterns of droplet dispersion: part i—mean quantities," 1995.

[29] P. Holmes, J. L. Lumley, G. Berkooz, and C. W. Rowley, *Turbulence, coherent structures, dynamical systems and symmetry*. Cambridge university press, 2012.

[30] A. F. Hussain, "Coherent structures and turbulence," *Journal of Fluid Mechanics*, vol. 173, pp. 303–356, 1986.

[31] L. Sirovich, "Turbulence and the dynamics of coherent structures. i. coherent structures," *Quarterly of applied mathematics*, vol. 45, no. 3, pp. 561–571, 1987.

[32] J. L. Lumley, *Stochastic tools in turbulence*. Courier Corporation, 2007.

[33] S. Terhaar, T. G. Reichel, C. Schrodinger, L. Rukes, K. Oberleithner, and C. O. Paschereit, "Vortex breakdown and global modes in swirling combustor flows with axial air injection," in *43rd AIAA Fluid Dynamics Conference*, p. 2602, 2013.

[34] J. L. Halpin, "Swirl generation and recirculation using radial swirl vanes," in *Turbo Expo: Power for Land, Sea, and Air*, vol. 78903, p. V03AT15A020, American Society of Mechanical Engineers, 1993.

[35] A. Sciacchitano and B. Wieneke, "Piv uncertainty propagation," *Measurement Science and Technology*, vol. 27, no. 8, p. 084006, 2016.

[36] A. Bay, F. Kıyıcı, and M. Perçin, "Effect of flare geometry on the flow field of radial-radial swirlers," in *Turbo Expo: Power for Land, Sea, and Air*, vol. 86007, p. V03BT04A047, American Society of Mechanical Engineers, 2022.

[37] F. Kıyıcı, "Experimental and numerical investigation of radial-radial swirlers under different confinement conditions," Master's thesis, Middle East Technical University, 2022.

[38] P. Weigand, W. Meier, X. R. Duan, W. Stricker, and M. Aigner, "Investigations of swirl flames in a gas turbine model combustor: I. flow field, structures, temperature, and species distributions," *Combustion and flame*, vol. 144, no. 1-2, pp. 205–224, 2006.

[39] P. Moise and J. Mathew, “Hysteresis and turbulent vortex breakdown in transitional swirling jets,” *Journal of Fluid Mechanics*, vol. 915, 2021.